

## **Influence of roughness on propeller performance with a view to mitigating tip vortex cavitation**

Savas Sezen\*, Dogancan Uzun, Osman Turan, Mehmet Atlar

*Department of Naval Architecture, Ocean & Marine Engineering, University of Strathclyde*

### **Abstract:**

This study explored the effects of uniformly and non-uniformly distributed biofouling roughness on hydrodynamic performance, particularly on the tip vortex cavitation (TVC) for model and full-scale marine propellers. The effect of roughness was investigated on a benchmark propeller belongs to the research catamaran, 'The Princess Royal'. The investigation also explored the potential use of the roughness effect to mitigate this propeller's tip vortex cavitation with uniform, inclined and non-uniform flow conditions. In the numerical calculations, DES (Detached Eddy Simulation) approach was used to simulate the cavitating flow around the propeller. The Schneer-Sauer cavitation model was used to model the sheet and tip vortex cavitation. An advanced meshing technique called V-AMR (Vorticity-based Adaptive Mesh Refinement) was proposed to model the TVC in the propeller slipstream. The modified wall-function approach was utilised to implement the roughness effects in the calculations using the experimentally obtained roughness functions based on one of the authors' recent study. The results showed that the velocity components decreased inside the tip vortex due to roughness, resulting in a pressure increase and TVC mitigation. The suction side of the propeller blade tips was found to be an effective roughness application area for the TVC mitigation with a moderate level of loss in the propeller efficiency. The findings indicated that the cavitation volume reduction, mainly due to the TVC mitigation, was by approximately 6-38%, with a 5-10% efficiency loss in the model scale, while these figures were 4-10% and 2-5%, respectively, for the full-scale propeller under the uniform and non-uniform flow conditions.

**Keywords:** Roughness, Biofouling, Cavitation, CFD, Tip Vortex Cavitation, Mitigation

## 1. Introduction

Marine transport is the backbone of global trade and the manufacturing supply chain since more than 80% of global trade is carried by sea. Although the global trade demand fluctuates on a year-by-year basis, statistics demonstrate that international maritime trade volume expanded over 320% from the 1970s to 2018 (UNCTAD, 2019). For this reason, commercial shipping is at the heart of world globalisation to meet the increased trade demand by increasing the ship numbers, sizes and propulsion power. However, one of the most adverse effects caused by the increasing shipping activities is the underwater radiated noise (URN) emissions (McKenna et al., 2012). Inevitably, the ship fleets' remarkable expansion has resulted in increased noise levels in the world's oceans, particularly in the low-frequency range (i.e. from 5Hz to 500Hz) (Hildebrand, 2004). The noise pollution caused by the ships is deemed one of the major threats influencing marine animals' survivability because the increased URN levels disrupt their natural habitat and cause local extinction (McKenna et al., 2012). Due to this fact, the concern for the adverse effects of shipping noise on marine animals have led to the development of non-mandatory guidelines to decrease the noise levels in the oceans (e.g., Det Norske Veritas - Germanischer Lloyd (DNV-GL) QUIET class, Registro Italiano Navale (RINA) DOLPHIN Class and IMO) (Bosschers, 2018).

A ship has different noise sources such as machinery & auxiliary engine noise, flow-induced noise around the ship's hull and its appendages, non-cavitating and cavitating propeller radiated noise. Amongst these sources, if present, cavitation on and off the propeller blades is a crucial noise source contributing to the overall radiated noise levels (Lorenzo et al., 2017).

As far as the propeller cavitation is concerned, it appears in many different forms (e.g., sheet, cloud, bubble, vortex cavitation) depending on the ship's operating condition and hydrodynamic design. Amongst these cavitation forms, the ship propellers generally operate in the presence of sheet and tip vortex cavitation or a combination of them (Bosschers, 2018; Asnaghi, 2018). Although the sheet cavitation on the propeller blades is considered to be more harmful than the vortex cavitation, the tip vortex cavitation (TVC), which usually occurs as the first type of cavitation on well-designed propellers, is also a significant noise source, particularly in the presence of bursting or collapsing phenomenon. This leads to a considerable increase in noise levels and hull-pressure fluctuations (Konno et al., 2002).

Therefore, TVC has deemed the main cavitation type controlled in the propeller design stage to mitigate URN (Asnaghi et al., 2020a).

There are different methods to modify, delay or mitigate the TVC on marine propellers. They can be identified as active and passive control methods (Yakushiji, 2009). In the active control methods, TVC can be suppressed by the polymer or water injection inside the tip vortex (e.g., Yakushiji, 2009; Fruman and Aflalo, 1989; Chahine et al., 1993; Platzer and Souder, 1981). On the other hand, as a passive control method, the most common approach is modifying the blade geometry by reducing the tip region's circulation to make the propeller tip unloaded. In this way, the circulation is decreased, and pressure inside the vortex is also increased (Carlton, 2018). In addition to this, the inclusion of additional geometry at the propeller blade tips, drilling holes and application of extra roughness on the propeller blades can be considered as alternative passive TVC mitigation methods (e.g., A. Feizi Chekab et al., 2013; Aktas et al., 2020; Asnaghi et al., 2020a; Asnaghi et al., 2020b). Amongst the different passive methods, the application of roughness on the propeller blades, which is the main interest of this study, becomes an appealing and suitable method to reduce the cavitation, hence propeller URN, particularly for retrofitting projects. In this regard, several experimental studies have been conducted using hydrofoil and propellers to understand the influence of roughness on the hydrodynamic performance of these submerged bodies and associated tip vortex flow.

In the past, Platzer and Souders, 1979 showed that roughness on the hydrofoil tip had a favourable impact on delaying the tip vortex cavitation inception. Katz and Galdo, 1989 conducted an experimental study in a towing tank using a rectangular NACA-66 hydrofoil in smooth and rough conditions. The experimental observations showed that the tip vortex's physical dimension was not affected considerably with the roughness application, while the pressure changed significantly. Thus, it was concluded that an increase in surface roughness enabled a reduction in the tip vortex strength. Johnsson and Rutgeresson, 1991 explored the influence of leading-edge roughness on the tip vortex roll-up phenomenon for different angles of attack. The results showed that the roughness applied on the pressure side and near the leading edge delayed the tip vortex cavitation, whereas it increased the drag up to 10% depending on the propeller operating condition, and hence efficiency loss was observed. Korkut and Atlar, 2012 performed another comprehensive experimental study. In these

authors' study, the hydrodynamic performance, including cavitation, and URN levels of the coated and uncoated propellers, were investigated in the Emerson Cavitation Tunnel. Considerable differences were not observed between coated and uncoated propellers in terms of cavitation. However, the noise levels decreased for the coated propeller at a higher advance coefficient, while the noise levels increased for the coated propeller compared to the uncoated one at lower advance coefficients. A recent and comprehensive experimental study was conducted by Svennberg et al., 2020 for an elliptical foil to investigate the effects of uniform and non-uniformly distributed roughness on cavitation inception and tip vortex flow. The cavitation inception properties of the foil were found similar by applying both uniform and non-uniformly distributed roughness, whereas the drag force was found to be higher for the non-uniformly distributed roughness in comparison with the uniformly distributed roughness.

Despite some favourable experimental reports for the influence of roughness on the propeller and hydrofoil cavitation in model scale, particularly to mitigate the TVC, similar investigations using the Computational Fluid Dynamics (CFD) in the model and full-scale are scarce. Tip vortex flow is a complex phenomenon with the challenging task of predicting its strength and size along its trajectory. It becomes further complicated with the application of roughness (Hunt et al., 1988; Asnaghi et al., 2020a). Krüger et al., 2016 investigated the effects of roughness on open water propeller performance under non-cavitating conditions using RANS and LES (Large Eddy Simulation) models. In their study, the roughness was modelled using both the wall function approach and physical dimple elements on the propeller blades by modelling a single propeller blade. The aim of their study was to explore the effects of propeller tip roughness and application area on the tip vortex flow. The results showed that strength of tip vortex decreased with the application of suction side tip roughness. Asnaghi et al., 2020a conducted a comprehensive numerical and experimental study to explore the impact of roughness on tip vortex and TVC with the use of roughness for an elliptical foil. Several roughness configurations and sizes were tested, and hydrodynamic performances were investigated. The roughness was modelled using a wall function approach and resolving the flow around the roughness elements with the LES method. These authors showed that the tip vortex cavitation inception could be decreased around 33% with a minimal drag increase (i.e. less than 2%). Following this study, the authors extended their investigation for

the marine propellers using CFD (Asnaghi et al., 2020b). The authors achieved the suppression of TVC considerably by keeping the efficiency loss as small as possible both in the model and full-scale propeller with the application of roughness on the strategic areas at the blade surfaces under the uniform flow conditions.

With the roughness application, the turbulence transition can be stimulated in the laminar boundary layer, and the near-wall flow structures can change significantly. The roughness elements also interfere with the tip vortex roll-up, which occurs due to the trailing vortex sheet and the interaction between the sheet and tip vortex cavitation. Thus, the roughness elements enable destabilisation and early breakdown of the tip vortex; hence, TVC and propeller URN mitigation. However, the roughness also causes efficiency degradation of a propeller. Yet, the important design task is to find a compromise between the hydrodynamic and hydroacoustic (or URN) performance optimisation for a propeller. Thus, the roughness's deteriorating impact on the propeller hydrodynamic performance characteristics (i.e., thrust, torque and efficiency) can be significantly reduced by applying the roughness to strategical areas on the propeller blades.

Within the above context, these authors' recent study explored the influence of uniformly distributed particular biofouling (barnacle) roughness on the hydrodynamic performance of a model-scale INSEAN E779A propeller under non-cavitating, cavitating and open water conditions using CFD. Also, the influence of roughness on the propeller URN levels was shown for the first time in the literature (Sezen et al., 2021). The noise reduction was achieved up to 10dB between the 1 and 2kHz frequency range at a very high cost of propeller efficiency loss (i.e., 25%) under cavitating conditions. The present study has extended this recent investigation further by exploring the effect of the similar roughness type, this time on the hydrodynamic performance and TVC of another benchmark propeller by considering the uniform and non-uniform roughness distributions in the model as well as in the full-scale.

Although a few studies have been conducted to investigate the influence of the roughness on tip vortex flow (e.g. Krüger et al., 2016), those studies are generally limited to the model scale propeller under non-cavitating conditions. Also, the investigation for the influence of roughness on the cavitating full-scale propeller is very scarce. As it is known, the tip vortex flows require detailed knowledge to understand where and how the tip vortex formation occurs, especially in a non-uniform wakefield, and hence its contribution to the propeller

URN. Also, to the best of the authors' knowledge, the influence of the roughness on propeller hydrodynamic performance and the potential use of this roughness to mitigate the TVC has not been explored yet under inclined and non-uniform flow conditions for both model and full-scale propellers. Therefore, this study aims to explore the effects of uniformly and non-uniformly distributed roughness on the hydrodynamic performance and TVC of a propeller in the model and full-scale, including the effect of the non-uniform wake and shaft inclination based on an existing benchmark research vessel propeller, The Princess Royal. The study also explores the strategic use of this roughness effect to mitigate the TVC of this propeller. The detailed investigation of the influence of roughness on TVC will help to incorporate the current CFD method with the propeller URN prediction model for the continuation part of this study.

Within the above-described aims, the cavitating flow around the model and the full-scale propeller was first solved using a DES approach together with the SST  $k-\omega$  turbulence model in Star CCM+ (Star CCM+, 2019). In the computations, the Schnerr-Sauer cavitation model, based on the reduced Rayleigh-Plesset equation, was used to model the sheet and tip vortex cavitation. To provide a better representation of the TVC in the propeller slipstream, the Vorticity-based Adaptive Mesh Refinement (V-AMR) technique developed by the leading author was employed. The hydrodynamic results and cavity pattern of the model and full-scale propeller were validated with the experimental and sea-trial data for a wide range of operating conditions for the smooth case. Later on, the roughness was included in the computations using the wall-function approach to model the influence of roughness with the modification of turbulent properties in the roughened regions. The roughness functions implemented in this study were obtained by Uzun et al., 2020. To explore the influence of uniformly and non-uniformly distributed roughness on the TVC and propeller global performance characteristics (i.e. thrust, torque values and efficiency), the model scale propeller operated under the uniform flow conditions at one of the operating condition. The tip vortex flow properties (e.g. variation of tangential velocity, turbulent kinetic energy, etc.) were examined in detail using the model scale propeller for several roughness configurations. The optimum roughness application area and roughness length scale were determined to mitigate the TVC and efficiency loss in the model scale. The determined optimum roughness application area and length scale were also used to show its effectiveness under uniform,

inclined and non-uniform flow conditions in the model and the full-scale propeller. The change in the propeller hydrodynamic performance and TVC mitigation were discussed in the presence of roughness.

## 2. Mathematical Model

### 2.1. Hydrodynamic Model

The numerical simulations were conducted using the commercial CFD solver (i.e. Star CCM+) (Star CCM+, 2019). The solver uses the finite volume method to discretise the governing equations (i.e. incompressible continuity and momentum equations). In the numerical calculations, the DES approach and the SST k- $\omega$  turbulence model were used to solve the propeller's flow field. DES is a hybrid modelling approach that combines the RANS features (Reynolds-averaged Navier Stokes) in some parts of the flow field and LES (Large Eddy Simulation) in the remaining parts of the flow field. In a DES approach, the boundary layer solution is provided by the RANS approach. In contrast, LES is utilised for the computational domain's free-flow region, particularly for the propeller wake. Thus, the DES approach can be a good compromise for capturing the flow details accurately that cannot be achieved by RANS. Also, it diminishes the computational cost of the LES solution (Spalart et al., 2006 and Star CCM+, 2019).

Cavitation is a formation of vapour bubbles in the liquid and occurs when the static pressure becomes equals and falls below the saturation pressure of vapour at a particular location. The commercial solver (i.e. Star CCM+) uses the homogeneous seed-based approach for cavitation modelling. In this approach, the seeds are spherical and uniformly distributed in the liquid, and they initially have the same radius. The Schneer-Sauer cavitation model based on the reduced Rayleigh Plesset equation was used to model the sheet and tip vortex cavitation. The phase transition between the vapour and liquid was provided using the VOF (Volume of Fluid) approach. The influence of bubble growth acceleration, viscous effects and surface tension effects are neglected in the selected cavitation model. The cavitation bubble growth rate can be estimated using the general Rayleigh Plesset equation's simplified formulation, as given in Equation 1.

$$\left(\frac{dR}{dt}\right)^2 = \frac{2}{3} \left(\frac{p_{sat} - p}{\rho_l}\right) \quad (1)$$

Here,  $R$  is the bubble radius,  $p_{sat}$  is the saturation pressure for a given temperature,  $p$  is the local pressure in the surrounding liquid,  $\rho_l$  is the liquid density. The cavitation number can also be calculated based on the propeller rotational speed as follows;

$$\sigma_n = \frac{p - p_{sat}}{\frac{1}{2}\rho_l(nD)^2} \quad (2)$$

where  $n$  is propeller rotational rate, and  $D$  is the propeller diameter.

The detailed information and equations about the cavitation modelling and VOF model can be found in the commercial solver user guide (i.e. Star CCM+, 2019) and Schnerr and Sauer, 2001.

## 2.2. Roughness Model

The flow around the roughness elements can be solved in two different approaches. In the first approach, the roughness geometries can be modelled physically and included in the computational domain as part of the surface. Although this approach gives a more realistic solution of the flow around the roughness elements, it requires a high number of grids for the accurate solution of the flow around them, which increases the computational cost of the numerical calculations. On the other hand, the second approach uses the roughness functions within the CFD software's wall function. Although this approach simplifies the geometry of roughness elements and the flow physics may not be modelled accurately compared to resolving the roughness elements itself, it is the more effective and computationally affordable approach to include the roughness effects in the calculations (Asnaghi et al., 2020b). Thus, in this study, the wall function approach was used to model the influence of roughness.

For the implementation of the roughness effects, the non-dimensional velocity profile in the log-law region can be written as;

$$U^+ = \frac{1}{\kappa} \ln(y^+) + B - \Delta U^+ \quad (3)$$

Here,  $\kappa$  is the von Karman constant,  $y^+$  is the non-dimensional normal distance from the wall,  $B$  is the smooth log-law intercept and  $\Delta U^+$  is the roughness function and it is dependent on the roughness Reynolds number ( $k^+$ ) which can be described as follows (Schultz and Swain, 2000).

$$k^+ = \frac{kU_\tau}{\nu} \quad (4)$$

where  $k$  is the roughness length scale,  $U_\tau$  is the frictional velocity and  $\nu$  is the kinematic viscosity. In this wall-function model, the roughness elements height needs to be lower than the height of the near-wall cell (i.e.,  $k^+ < y^+$ ). Also, the selected  $y^+$  value needs to be higher than 30 to impose the influence of roughness on the numerical calculation (Star CCM+, 2019).

The flow over the rough wall can be divided into three different flow regimes: hydraulically smooth, transitionally rough and fully rough, depending on the roughness Reynolds number. When the roughness elements are small and embedded in the viscous sublayer, the flow regime is assumed as hydraulically smooth. In this flow regime, the frictional drag is not affected by the roughness elements and the roughness function (i.e.,  $\Delta U^+$ ) becomes zero. If the roughness elements partially penetrate beyond the viscous sublayer, the flow regime is called a transitional regime. When most of the roughness elements penetrate the linear sublayer, the flow regime becomes fully rough. Thus, the skin friction becomes independent of the Reynolds number, and viscous effects start to be no longer important (Flack and Schultz, 2010; Schultz and Swain, 2000).

Roughness functions ( $\Delta U^+$ ) related to varying rough surfaces are recommended in the literature to reflect its effects on the hydrodynamic performance of ship hull and propeller. The widely used roughness functions can be classified into two groups: inflectional-behaviour functions with three flow regimes and single expression functions. The single expression functions are generally referred to as Colebrook/Grigson-type, initially proposed by Colebrook, 1939 and adopted by Grigson, 1992 (Andersson et al., 2020). The Colebrook/Grigson-type roughness functions are based on a single definition to identify the roughness function given below.

$$\Delta U^+ = \frac{1}{\kappa} \ln(1 + k) \quad (5)$$

The roughness functions used in this study were obtained by Uzun et al., 2020. In the authors' study, the flat plates covered with 3D printed artificial barnacle tiles in different sizes, coverages, and settlement patterns were towed in towing tank. Then, roughness functions were derived based on the overall method proposed by Granville (1978). The obtained

barnacle type roughness functions (or biofouling roughness functions) showed good agreement with Colebrook type roughness functions of Grigson, 1992.

Table 1 shows the representative roughness length scales and corresponding configurations with different barnacle sizes and coverage densities. In the CFD model, roughness functions provided in Uzun et al., 2020, were implemented within the CFD solver's wall function. Detailed information about the roughness functions can be found in the study of Uzun et al., 2020. In Table 1, Mix and NS Mix are surface names obtained from the study of Uzun et al., 2020,  $h$  is barnacle height (mm),  $k_G$  is the representative hydrodynamic roughness length scale ( $\mu\text{m}$ ) that give the same roughness Reynolds numbers with corresponding roughness function values of Grigson, 1992. It should be noted that these representative hydrodynamic roughness length scales,  $k_G$ , are not a function of measurable surface properties and may be termed as experimentally obtained equivalent roughness height.

**Table 1.** Representative roughness length scales of test surfaces implemented in this study (Uzun et al., 2020).

Test Surfaces	Surface Coverage (%)	Barnacle Height $h$ (mm)	Representative roughness length scale $k_G$ ( $\mu\text{m}$ )
Mix	10	5, 2.5, 1.25	94
NS Mix	10	5, 2.5, 1.25	136
Mix	20	5, 2.5, 1.25	337
NS Mix	20	5, 2.5, 1.25	408

### 3. Test Case Description and Test Matrix

In the numerical calculations, the Newcastle University's (UNEW) Deep-V type catamaran research vessels' propeller (i.e., The Princess Royal), which is the recently introduced benchmark propeller, was selected (Atlar et al., 2013). The reason behind this was the data available from the extensive cavitation tests and URN measurements in the model and full-scale with this vessel through the FP7-SONIC project (Suppression Of underwater Noise Induced by Cavitation, (SONIC, 2012)) and currently ongoing round-robin (RR) test campaign organised by HTF (Hydro Testing Forum). Hence, the cavitation observations and propeller URN data, including sea trial data, are available in the model and full-scale for the selected propeller. The main characteristics of the propeller geometry is given in Table 2. In Table 2, P/D is pitch ratio.

**Table 2.** *The main parameters of the propeller (Atlar et al., 2013).*

Parameters	Full-Scale	Model Scale
Diameter, $D$ (m)	0.75	0.22
$P/D$ at 0.7R		0.8475
Expanded Blade Area Ratio		1.057
Blade Number, $Z$		5
Rake ( $^\circ$ )		0
Skew ( $^\circ$ )		19

Table 3 shows the selected uniform, inclined and non-uniform operating conditions for the model and full-scale propeller. The operating conditions were determined according to the experiments conducted in the University of Genoa Cavitation Tunnel (UNIGE) in the scope of the round-robin (RR) test campaign for The Princess Royal propeller (Tani et al., 2019b). In Table 3,  $\beta$  is the shaft or inclination angle ( $^\circ$ ),  $J$  is advance ratio,  $n$  is propeller rotational rate (rps),  $\sigma_N$  is the cavitation number based on the propeller rotational rate,  $\nu$  is kinematic viscosity ( $\text{m}^2/\text{s}$ )

**Table 3.** *Test cases under uniform and inclined flow conditions.*

	Loading Condition	Shaft Angle ( $\beta$ , $^\circ$ )	$J$ (-)	$n$ (rps)	Reynolds Number ( $Re = \frac{nD^2}{\nu}$ )	$\sigma_N$ (-)
MODEL SCALE	C2	0	0.4	35	$1.58 \times 10^6$	1.30
	C6	0	0.5	35	$1.58 \times 10^6$	1.13
	C8	5	0.4	35	$1.58 \times 10^6$	1.30
	C12	5	0.5	35	$1.58 \times 10^6$	1.13
FULL SCALE	C13	0	0.4	19.025	$1.00 \times 10^7$	1.06
	C14	0	0.5	19.025	$1.00 \times 10^7$	1.06

In addition to uniform and inclined flow conditions, the numerical computations were also performed in the presence of a simulated non-uniform wakefield based on the measured wakefield data in the Ata Nutku Towing tank of Istanbul Technical University (Korkut and Takinaci, 2013). In this way, the realistic flow conditions were modelled for the Princess Royal propeller. The simulated wakefield was achieved iteratively using a 2D wire mesh and LDV flow measurement device in the UNIGE tunnel until a good agreement was achieved with the target wake (i.e. towing tank wake data) (Tani et al., 2019a). Figure 1 shows the simulated

wake and the target wake. As shown in Figure 1, there are missing values on the left side of the velocity distribution obtained by the cavitation tunnel. This is because of the inaccessible areas by the LDV beams in the cavitation tunnel.

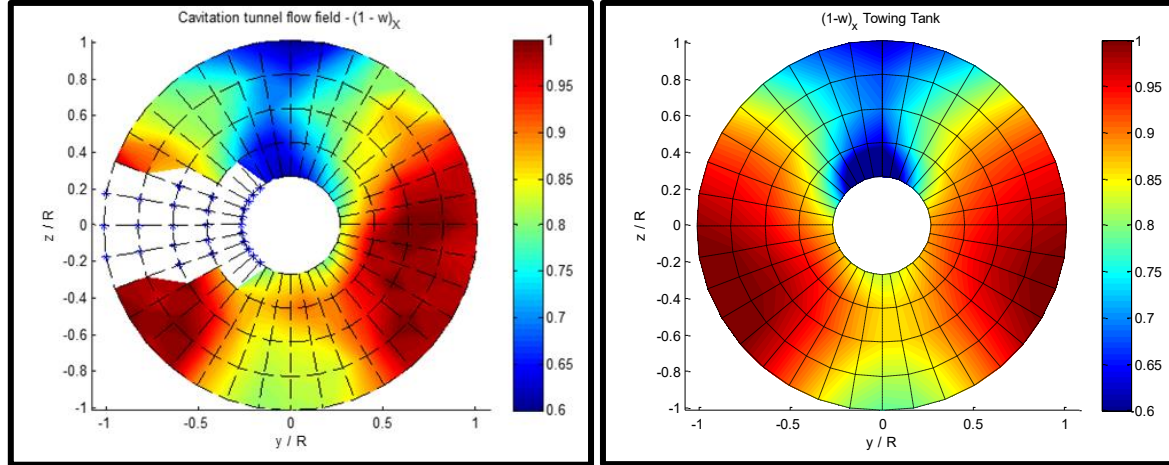


**Figure 1.** Nominal wakefield at the propeller plane (Left: simulated wakefield in the cavitation tunnel, right: target wakefield measured in the towing tank) (Tani et al., 2019a).

The operating conditions are also given in Table 4 for both model and full-scale propeller under non-uniform wakefield. In Table 4,  $V_S$  is the ship speed (knot),  $K_Q$  is non-dimensional torque coefficient of the propeller.

**Table 4.** Test cases under the non-uniform wakefield.

	Condition	Engine RPM	$n$ (rps)	$V_S$ (knot)	$10K_Q$	Reynolds Number ( $Re = \frac{nD^2}{\nu}$ )	$\sigma_N$
Model Scale	C15	2000	35	15.11	0.318	$1.58 \times 10^6$	1.07
Full Scale (Sea Trial)	C16	2000	19.025	15.11	0.318	$1.00 \times 10^7$	1.07

The four different representative roughness length scales, given in Table 1, were applied on the propeller blades with uniform and non-uniform roughness distributions to find the optimum roughness area. Figure 2 shows the roughness application areas on the propeller blades with black colour. Also, Table 5 summarises the location of roughness patterns. Here,  $r/R$  is the section of blades.

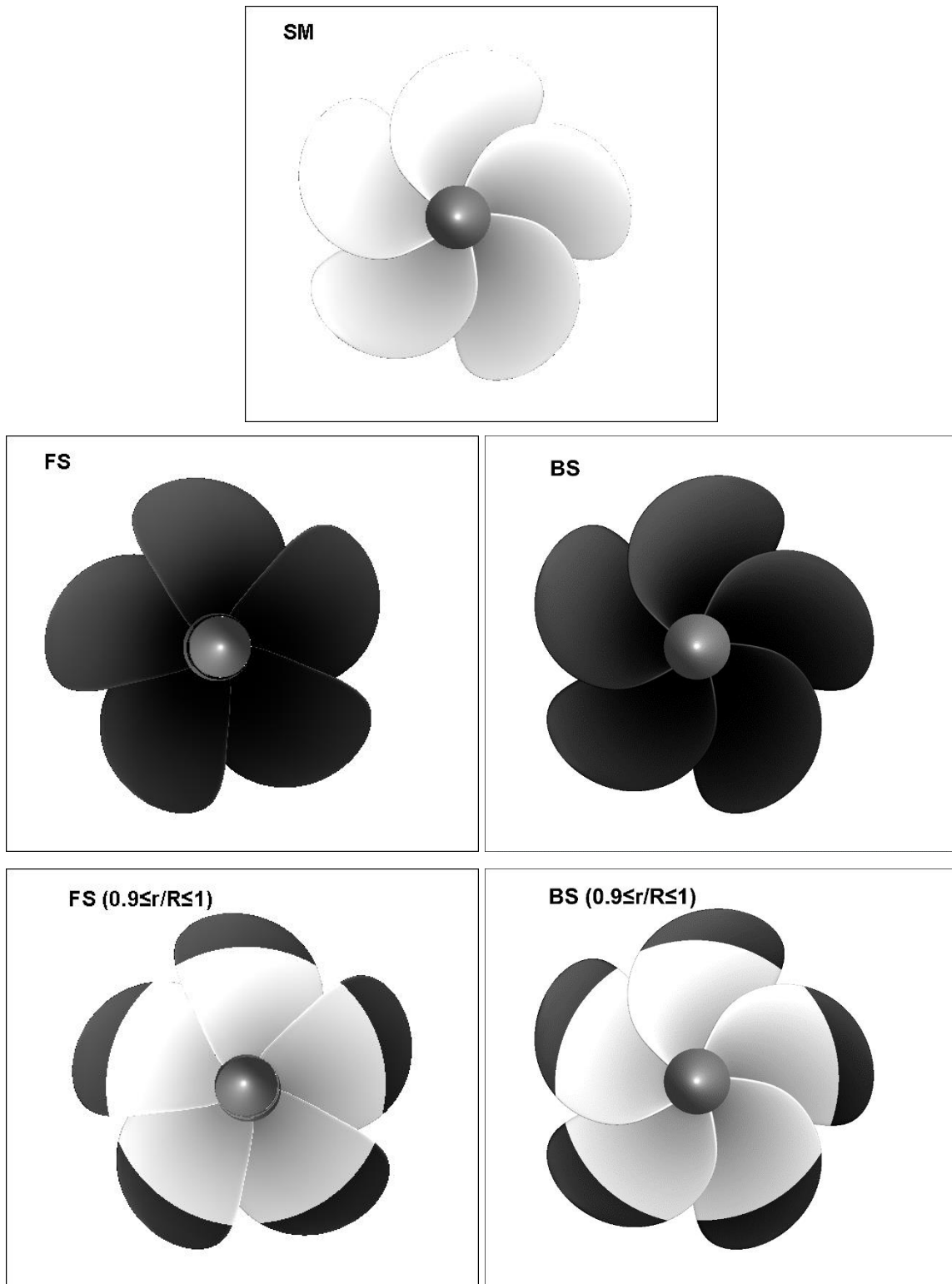


**Figure 2.** Representation of roughness application areas on the propeller blades.

**Table 5.** *The explanations of roughness application area on the propeller blades.*

ID.	The roughness application area
SM	Blades are smooth.
FS+BS	Face and back side of the blades
FS	Face side of the blades
BS	Back side of the blades
FS09+BS09	Face and back side of the blades between $0.9 \leq r/R \leq 1$
FS09	Face side of the blades between $0.9 \leq r/R \leq 1$
BS09	Back side of the blades between $0.9 \leq r/R \leq 1$

## 4. Numerical Modelling

### 4.1. Computational Domain & Boundary Conditions

Figure 3 shows the computational domain used in the numerical calculations in the model scale. In the numerical calculations, all propeller blades were modelled to reflect the realistic test configuration both in model and full-scale. The computational domain dimensions were set according to the measurement section of the cavitation tunnel dimensions. The test section's total length is around 2.2m, and it has a 0.57 x 0.57 m square test section. Hence, the computational domain's upstream was extended around 2.5D, whereas the domain's downstream length was set to 7.5D. The radial distance of the computational domain was set to 0.57m. The X-direction was identified as velocity inlet, while the negative X direction was defined as pressure outlet. The pressure gradient at the outlet of the computational domain was set to zero. The remaining surfaces of the domain were defined as a no-slip wall. No-slip boundary condition was also used for the propeller blades, shaft and hub. The computational domain was divided into two different regions (i.e., static and rotating region). The rotating region was created around the propeller blades to provide the propeller rotational motion using a cylindrical body. The rotating and static regions are connected with the internal interfaces.

The computational domain was created to replicate the free field conditions for the full-scale propeller. In this regard, the upstream and downstream of the domain were set to 4D and 16D. The radial distance was set to 5D. The remaining boundary conditions were taken the same with the computational domain of the model scale.

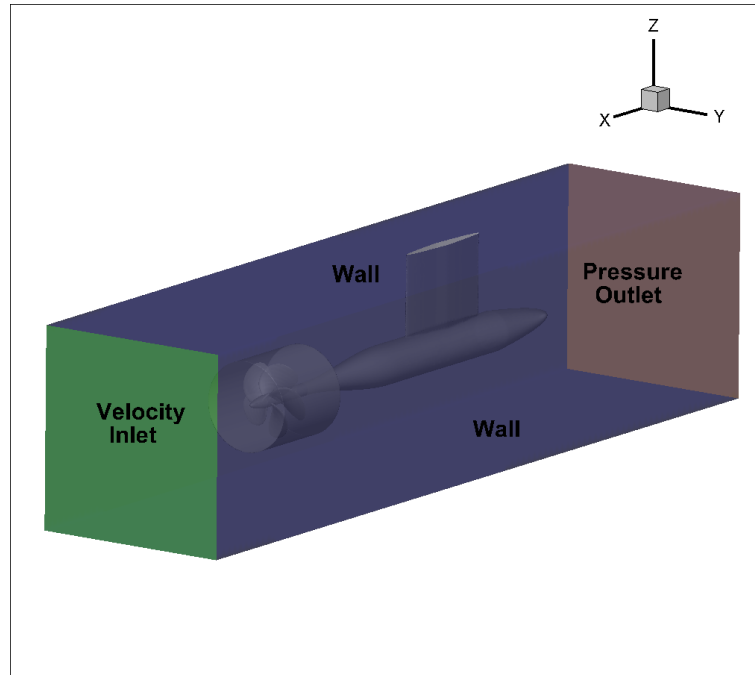


**Figure 3.** Perspective view of the computational domain for the model-scale propeller.

#### 4.2. Grid Structure

The quality of the grid structure is important for an accurate solution with less amount of dissipation. Hence, the grid should be sufficient enough to solve the complex flow phenomena around the propeller blades under cavitating conditions. As the tip vortex flow solution is more dependent on the grid resolution, the numerical dissipation should be significantly reduced in the propeller slipstream by increasing the grid resolution, particularly around the tip vortex area. However, the application of fine grid resolution in the entire propeller slipstream would increase the total element count and hence the solution's computational cost. It consequently becomes unpractical for numerical applications. Thus, to decrease the total element count and solve the tip vortex region's flow field accurately, advanced meshing techniques (e.g. Adaptive Mesh Refinement) can be an alternative and practical way to decrease the computational cost of the solution. In this technique, the fine grid resolution can be applied locally to resolve the tip vortex flow according to user-based field functions. For this purpose, the first author of this study introduced the more computationally affordable AMR procedure called Vorticity based Adaptive Mesh Refinement Technique (V-AMR) for model and full-scale propeller applications (Sezen and Atlar, 2021; Sezen et al., 2021). In the V-AMR technique, the vorticity based (i.e., gradient quantity)  $Q$  criterion was used as a refinement criterion. In order to determine the required cell size in

the tip vortex region to observe the TVC, the recommendations of the crucial studies were taken into account (e.g., Kuiper, 1981 and Asnaghi, 2018). In this regard, a series of cavitation tests were conducted using the model scale propeller by Kuiper, 1981. The author explored the relationship between cavitation number and core radius. The experimental results showed that the core radius was around 0.25mm at the cavitation inception. Another comprehensive numerical study was also conducted by Asnaghi, 2018 for the accurate solution of the tip vortex flow for an elliptical foil. Also, the extensive numerical study has been recently performed using different grid sizes in the tip vortex (Sezen and Atlar, 2021). Consequently, the grid size in the vortex region was set to 0.2mm for the model scale propeller. In full-scale propeller, the tip vortex diameter is larger than the those of model scale propeller; hence, the grid size will not have to be same order with model scale propeller. However, it should be similar order relative to the propeller. Therefore, the grid size in the vortex region was enlarged with the scale ratio (*i. e.*,  $\lambda = 3.41$ ) and it was set to 0.68mm for the full-scale propeller.

The proposed V-AMR procedure consists of two stages. At the 1<sup>st</sup> stage of the procedure, the tip vortex trajectory is determined using a relatively coarse grid when the flow field converges with the initial mesh. The tip vortex trajectory can be identified based on the threshold value of the  $Q$  criterion. Following this, the new mesh table is created in all directions using the user-based field functions. In this way, the local mesh refinements provided by the user based field functions show the areas where the magnitude of the vorticity (or  $Q$  criterion) is higher than the selected threshold value. When the flow field converges with the 1<sup>st</sup> stage of the V-AMR procedure (*i.e.*, after a few propeller rotations), the 2<sup>nd</sup> stage of the V-AMR procedure can be adopted with the new threshold value of  $Q$  criterion. The advantage of the two stages V-AMR procedure application is to decrease the total element count in the numerical solver and hence the computational cost.

The unstructured grid with the trimmer mesh algorithm was created to discretise the computational domain using the Star CCM+ automated mesh tool (Star CCM+, 2019). The suitable transitions and mesh alignment was adopted between rotating and static region to remove the additional numerical issues. The high cell quality and uniform mesh in all directions were imposed by avoiding highly skewed cells in the computational domain. The full-scale propeller grids were scaled from the model scale grids with additional mesh

refinements. Figure 4 indicates the propeller blades' grid structure with the local mesh refinement using the V-AMR procedure. Also, the grid properties are given for both the model and full-scale propeller, as shown in Table 6.

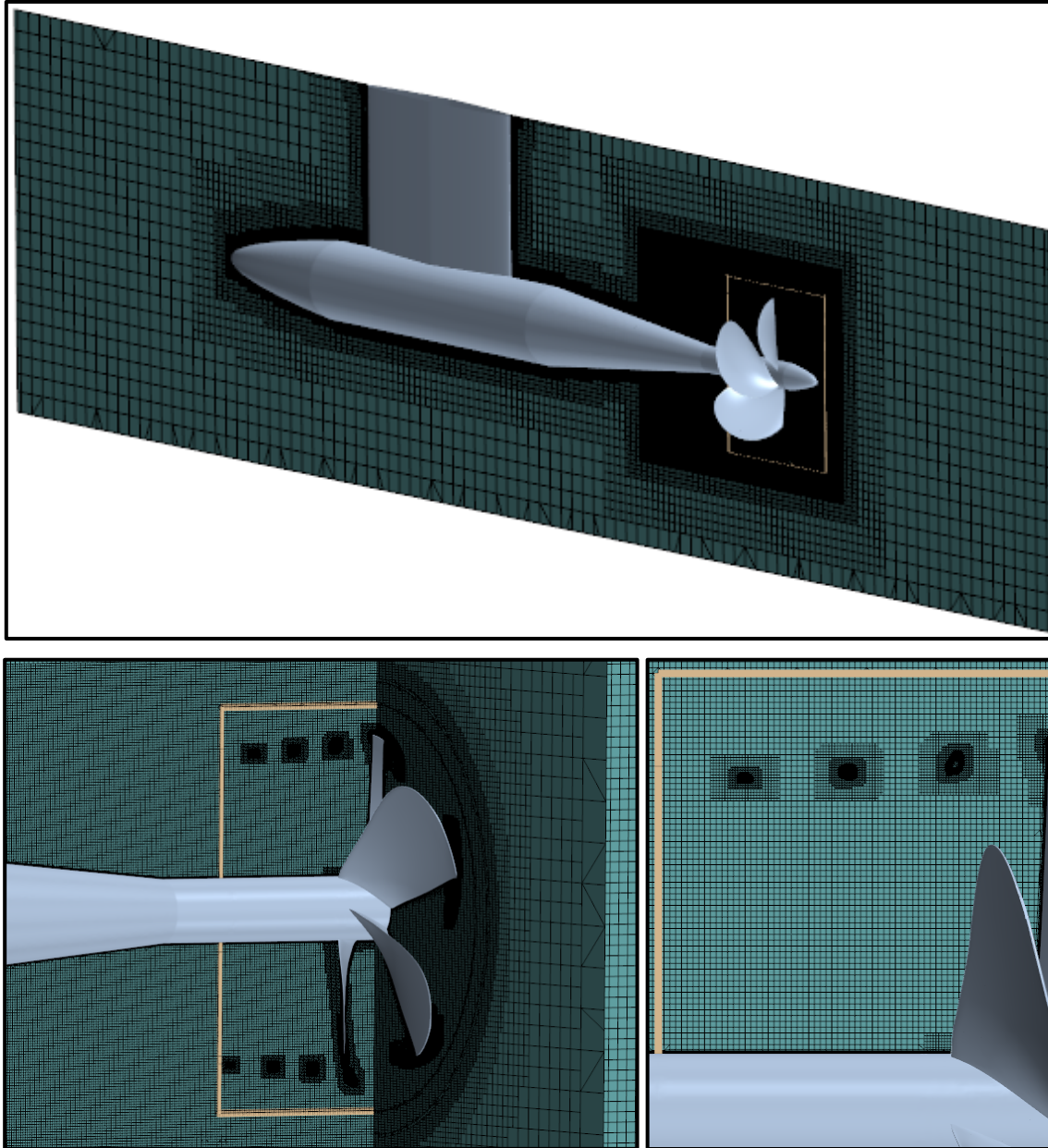


**Figure 4.** Grid structure around the propeller blades.

**Table 6.** Grid properties for both model and full-scale propellers.

	1 <sup>st</sup> V-AMR size (mm)	2 <sup>nd</sup> V-AMR size (mm)	Total Number of Cells (Million)
Model Scale	0.40	0.20	23.5
Full Scale	1.36	0.68	27

### 4.3. Solution Strategy

In the numerical calculations, the SST  $k-\omega$  turbulence model was used with all  $y^+$  wall treatment methodology for the DES approach. The DDES (Delayed Detached Eddy Simulation) variant of the DES approach was used in the numerical calculations. The second-order scheme, which is more suitable and advisable for the DES approach, was used to discretise the convection term. Additionally, the second-order implicit unsteady scheme was employed for the time discretisation with the  $0.5^\circ$  of propeller rotational rate for each test case. The SIMPLE algorithm (Semi-Implicit Method for Pressure-Linked Equations) was utilised for the velocity and pressure coupling. In this approach, the discretised momentum pressure correction equations are solved implicitly (Star CCM+, 2019). The average  $y^+$  value was calculated between 250 and 290 depending on the operating condition for the model scale propeller. It was also calculated between 380-420 depending on the operating condition for the full-scale propeller. In this way, the roughness effects were imposed on the calculations by satisfying the criteria of the wall function approach (i.e.,  $k^+ < y^+$ ).

The sliding mesh or Rigid Body Motion (RBM) technique was used to model the propeller rotational motion. Nevertheless, the Moving Reference Frame (MRF) approach, which is used to solve the problem in a steady-state condition, was also used at the initial stage of the solution with the RANS approach in a steady manner to accelerate the convergence process. In the unsteady approach, the DES approach and RBM technique were activated for the solution's remaining part. The simulations were started with the  $1^\circ$  of propeller rotational rate to reduce the possible numerical issues created by the cavitation and facilitate the stabilisation of the flow conditions. After a few propeller rotations, the time step was reduced to  $0.5^\circ$  of propeller rotational rate. The inner iteration was set to 8 and 10 for model and full-scale propellers, respectively. During the simulations, the hydrodynamic coefficients and velocity field were checked to determine the convergence of the solution. Once the simulations converged, the mean thrust, torque coefficients, total cavitation volume, velocity field were computed based on the time-averaged data. The simulations were run around 10 propeller rotations by taking the convergence of the solution into account.

### 5. Results

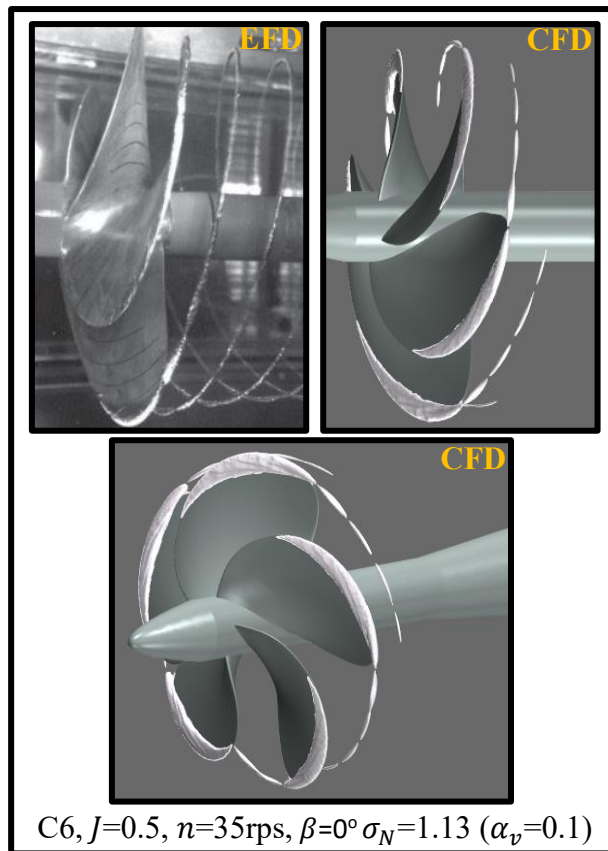
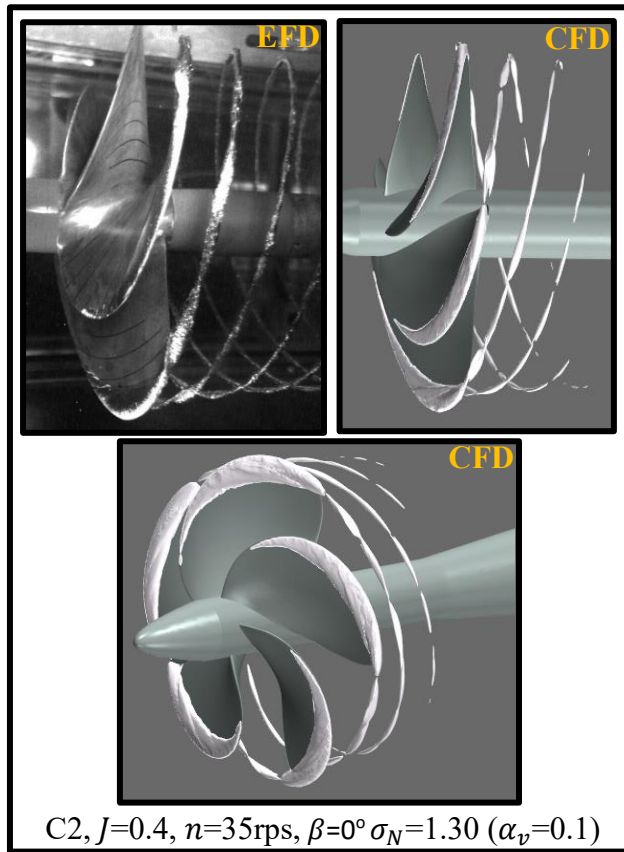
In this section, the cavitation patterns and propeller hydrodynamic performance characteristics were validated with the experimental and sea trial data in smooth conditions.

Following this, the uniformly and non-uniformly distributed roughness were applied on the propeller blades in the model scale, and the most effective roughness area and length scale were determined. The variation of flow properties in the tip vortex, cavitation volume reduction and efficiency loss was explored for model and full-scale propellers in the presence of roughness.

### 5.1. Smooth Propeller

Figure 5 compares cavitation extensions between the numerical computation and experimental observation in the model scale under uniform and inclined flow conditions. Here,  $\alpha_v$  is the vapour volume fraction. As shown in Figure 5, C2, C6, C8 and C12 show similar cavitation phenomena and dynamics with slight differences in the cavitation extensions. Even though the regular and stable tip vortex cavitation is observed for all conditions, the tip vortex cavitation diameter is stronger in C2 and C8 conditions than C6 and C12 because of the higher blade loading. With an increase in blade loading, the sheet cavitation is extended towards the inner radii. The stable tip vortex cavitation dynamics in the propeller slipstream could be observed with the V-AMR technique in the numerical calculations. The numerical results agree with the experimental observations with slight differences in the sheet cavitation extension towards the inner radii.

Table 7 shows the comparison of thrust coefficients ( $K_T$ ) obtained by CFD and experiment. The differences were found at around 7%. The reason being is that the thrust coefficient identity approach, which corresponds to  $J=0.4$  and  $J=0.5$ , was used during the measurements at the UNIGE tunnel, whereas the CFD calculations were conducted according to the  $J$  identity. Also, the cavitation patterns and propeller performance characteristics showed good agreement at the same conditions with those of other experimental data obtained by different facilities in the scope of the round-robin (RR) test campaign (e.g., Tani et al., 2020).



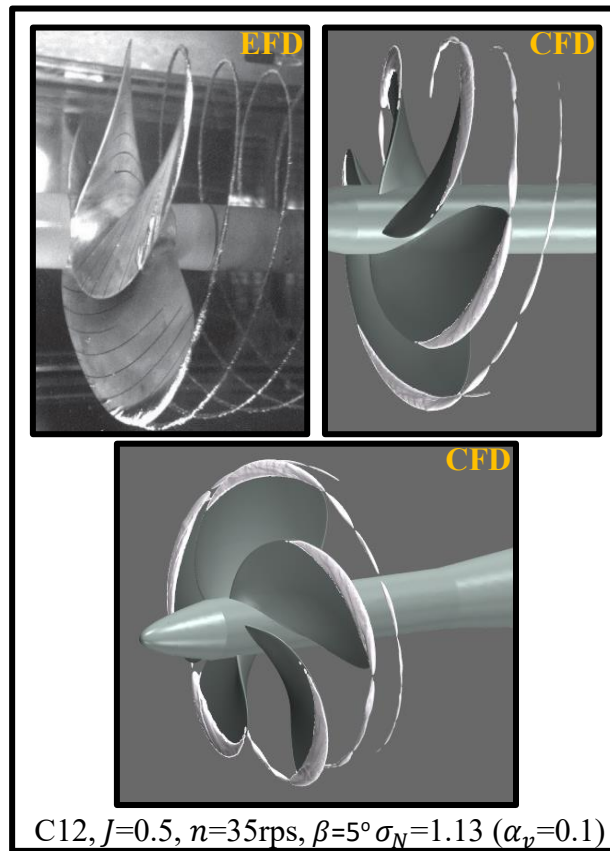
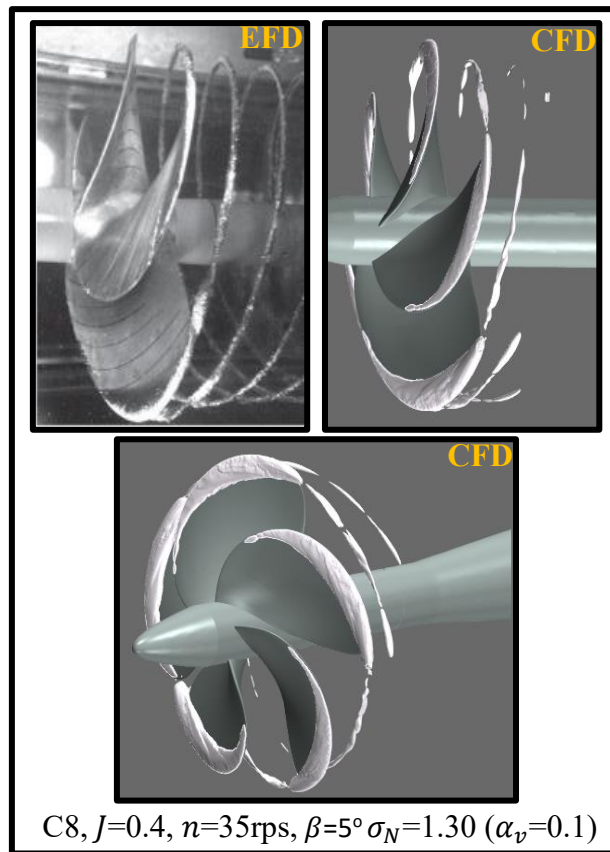


**Figure 5.** Comparison of cavity patterns between CFD and experiment (EFD).

**Table 7.** Comparison of thrust coefficients between CFD and experiment.

Condition	$K_T$ (CFD)	$K_T$ (EFD)
C2	0.263	0.244
C6	0.206	0.191
C8	0.256	0.245
C12	0.207	0.192

The sheet and tip vortex cavitation obtained by CFD, model experiments and sea trial data were also compared for both model and full-scale propeller under the non-uniform flow conditions (i.e., conditions 15 and C16) as shown in Figure 6. The large extent of suction side sheet cavitation (i.e., around 25-30% of the blade area) was observed during the sea trials. As shown in the model experiment, two tip vortex structures are emanating the propeller blade tips. The first tip vortex structure occurs because the sheet cavity breaks up, and it is formed as an unstructured and cloudy vortex. In contrast, the second vortex formation starts at the trailing edge's (inner) end with a more distinct vortex core. The close interaction between the two vortex structures is present. These cavity dynamics were also somewhat observed in the numerical calculations using the V-AMR technique for the model and full-scale propeller. Additionally, the complex cavity dynamics associated with the cloudy appearance observed in the sea trial could not be observed in the numerical calculations both in the model and full-scale and model experiments. It is to be noted that the cavitation extension could not be compared at each blade angle between the CFD, model experiment and sea trial due to the lack of experimental and sea trial observation.

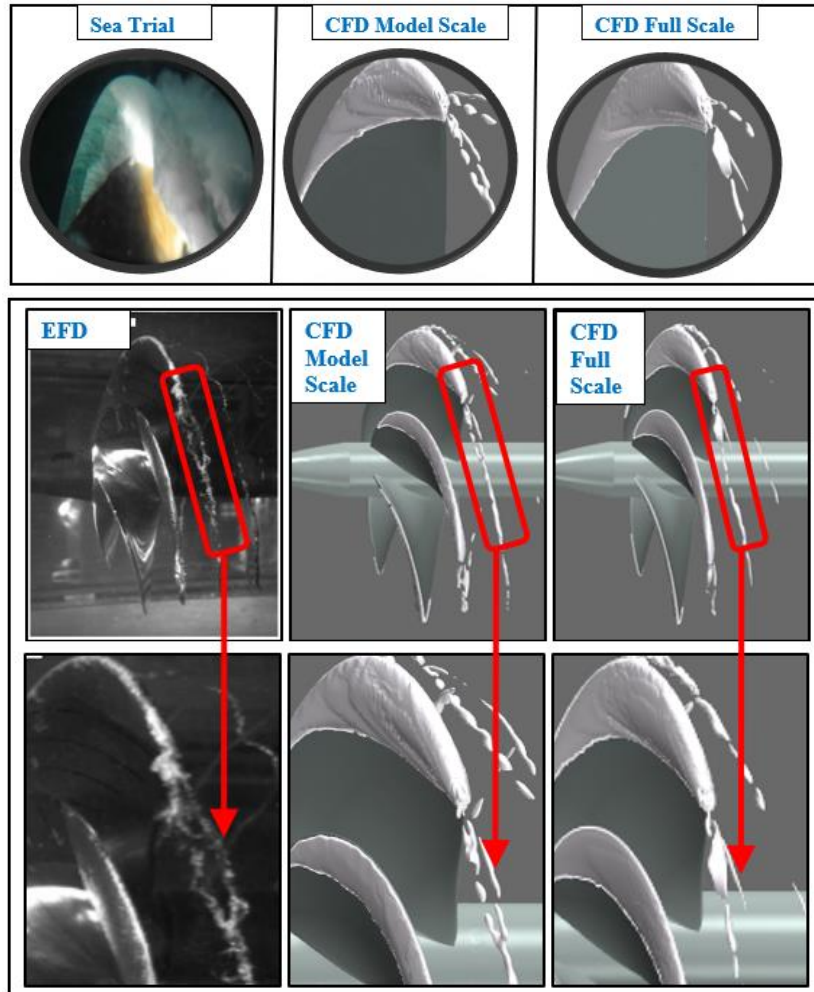


**Figure 6.** Comparison of cavity patterns between CFD, model experiment (EFD) and sea-trial data at C15 and C16 ( $\alpha_v=0.1$ )  
 (The sea trial and experimental cavitation observations were taken from Sampson et al., 2015, Tani et al., 2019a, respectively).

Table 8 shows the comparison of the torque coefficients between the CFD, model experiment and sea-trial data. In the model experiment, the propeller operational condition was defined according to the torque coefficient and cavitation number identity to represent the sea trial condition. As shown in Table 8, the difference between the CFD and sea trial data was found around 13% in torque coefficients. The discrepancy between CFD and sea-trial data might be due to the dissimilarities of the wake distribution used in the numerical calculation.

**Table 8.** Comparison of torque coefficients between CFD, experiment (EFD) and sea trial data.

Condition	Parameter	CFD	Sea Trial	EFD
C15 (Model Scale)	$10K_Q$	0.361	-	0.318
C16 (Full Scale)	$10K_Q$	0.362	0.318	-

## 5. 2. Rough Propeller

### 5.2.1 Model Scale Propeller

#### 5.2.1.1 Variation of flow details in the tip vortex with the roughness

The tip vortex flow around the marine propeller was investigated to understand the influence of roughness on the flow details inside the tip vortex in model scale at Condition 6. For this reason, the face and backside of the propeller (i.e., FS+ BS) were covered with uniformly distributed roughness, which has different representative roughness length scales as given in Table 1. The axial plane was located in the propeller slipstream to investigate the roughness effects on the velocity components inside the tip vortex, as given in Figure 7. The axial and tangential velocity profiles were extracted from the black-dashed lines between the purple-solid lines shown in Figure 7.

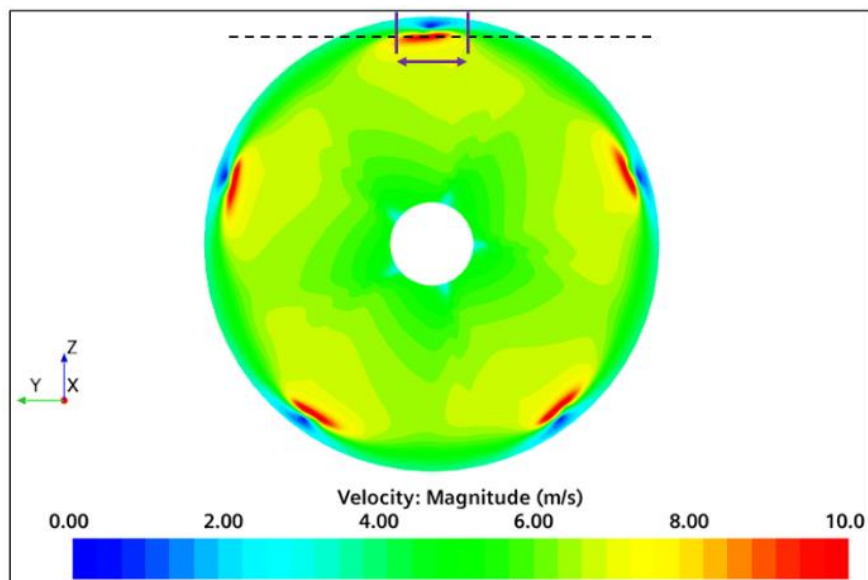


**Figure 7.** The velocity field in the propeller slipstream at  $x=-0.031$  m

Figure 8 compares the axial and tangential velocity profiles between the smooth and roughened conditions. The axial and tangential velocities were normalised with the inflow velocity. The vortex core diameter can be considered the distance between the maximum and minimum velocities' locations in the azimuthal velocity profiles. As shown in Figure 8, the axial and azimuthal velocities' magnitudes reduced in the presence of roughness compared to the smooth condition, particularly around the vortex core. Interestingly, velocity profiles outside the vortex core are similar both in smooth and roughened conditions. The vortex core radius and axial velocity peak slightly change with the roughness application. The increase in the

roughness length scale causes more reduction in the velocity magnitudes. Having a lower axial and tangential velocity will consequently increase the pressure inside the tip vortex.

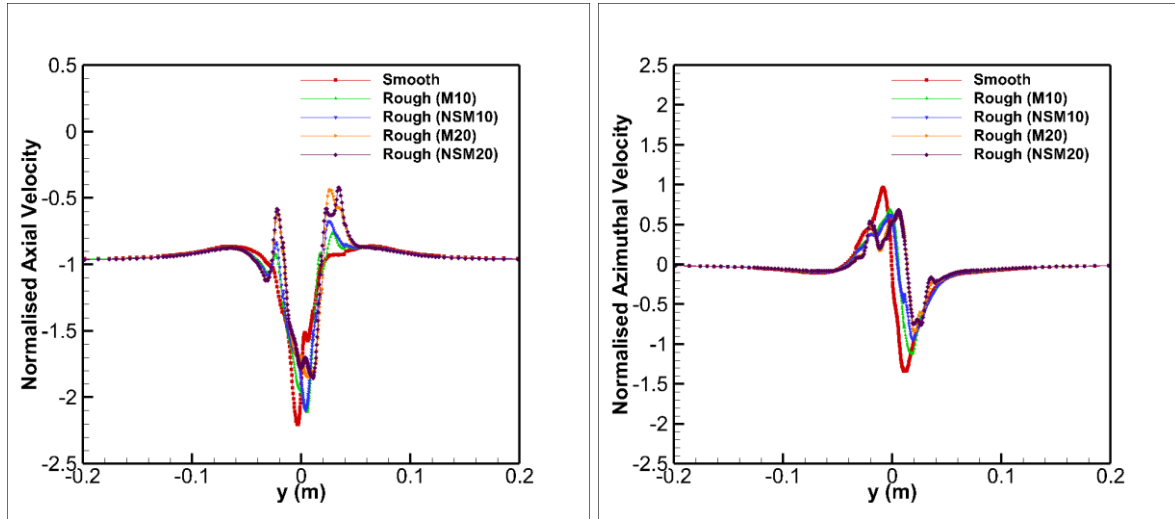


**Figure 8.** The change in normalised axial and azimuthal velocities with the roughness.

Figure 9 indicates the turbulent kinetic energy around the vortex region both in smooth and rough conditions. As shown in Figure 9, the turbulent kinetic energy's maximum value appears at the vortex core centre for the rough and smooth conditions. The additional viscous stresses between the tip vortex and roughened blade surface lead to transforming the vortex's circumferential momentum into turbulent kinetic energy. With an increase in roughness length scale, turbulent kinetic energy increases considerably compared to the smooth condition.

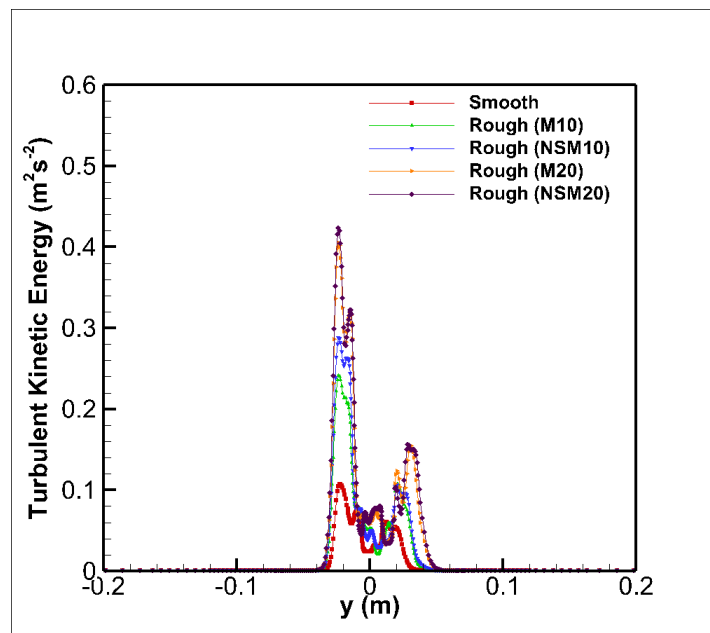


**Figure 9.** The change in resolved turbulent kinetic energy with the roughness (the data was obtained at the location as given in Figure 7)

### 5.2.1.2. Determination of optimum roughness application area and roughness length scale

As shown in the previous chapter, the roughness elements interfere with the tip vortex's velocity and pressure field. It enables a decrease in the velocities' magnitude (i.e., increase in pressure) inside the vortex core. However, this favourable impact on tip vortex flow negatively affects the blade sections' hydrodynamic characteristics. In the presence of roughness, the blade sections' drag increases, whereas the lift of the blade sections decreases due to reduced circulation distribution around the propeller blades. Inevitably, this will cause a decrease in thrust value and an increase in torque, resulting in efficiency loss for the propeller. Due to this reason, the roughness application area should be optimised to find a compromise between TVC mitigation and efficiency loss.

In order to find the optimum location on the propeller blades, the uniformly and non-uniformly distributed roughness configurations with different length scales were applied in the model scale at Condition 6 as given in Table 1 and Table 5. Figure 10 shows the change in cavitation volume and efficiency loss with different roughness configurations and length scales concerning the smooth condition. In all configurations in Figure 10, the roughness increases the torque coefficient. The maximum increase is found around 35% at the highest roughness length scale (i.e., NSM20) when the uniformly distributed roughness is applied at both sides of the propeller blades (i.e., FS+BS configuration). Yet, the roughness decreases the thrust coefficient for all configurations, except FS and FS09+BS09 configuration. The maximum thrust decrease is also found around 24% for BS configuration. When the roughness is applied on the blades using the FS and FS09+BS09 configurations, the thrust coefficient increases around 3%. However, the torque coefficient's substantial increase results in efficiency loss even if the propeller thrust increases. When the roughness is only applied on the propeller blade tips (i.e., FS09, BS09 and FS09+BS09 configuration), the thrust and torque coefficient change are smaller than those of other configurations.

As expected, the application of the uniform roughness on the propeller blades shows the maximum performance degradation even if the cavitation volume reduction is higher than those of other configurations with an increase in roughness length scale. On the other hand, the non-uniformly distributed roughness has a favourable impact on the propeller efficiency loss. In this regard, applying the roughness only on the propeller blade tips (i.e., FS09, BS09 and FS09+BS09) reduces the efficiency loss. Amongst these configurations, the roughness

application only on the suction side (or backside) of the propeller blade tips (i.e., BS09) enables a significant reduction in efficiency loss. In this way, the efficiency loss can be decreased by approximately 20-32% depending on the roughness length scale compared to uniformly distributed roughness on all propeller blades (i.e., FS+BS configuration).

Regarding the cavitation volume change, applying the roughness on the propeller blades reduces the cavitation volume for all configurations with respect to the smooth case, except the FS and FS09. Remarkably, applying the roughness on the pressure side (or face side) (i.e., FS and FS09) shows the opposite trend and increases the cavitation volume. This opposite trend becomes more pronounced with an increase in roughness length scale. The reduction of cavitation volume is mainly due to the mitigation of TVC as the roughness increases the pressure inside the vortex. This TVC mitigation further increases with an increase in the roughness length scale.

The several roughness application areas enable understanding the influence of roughness on the propeller efficiency and cavitation volume reduction. To achieve a compromise between the propeller efficiency loss and the cavitation volume reduction, the BS09 is selected as an optimum roughness application area. Regarding the optimum representative roughness length scale ( $k_G$ ), the change in the efficiency loss between  $k_G = 337\mu m$  and  $k_G = 408\mu m$  roughness length scales is found below 1%. Yet, the cavitation volume reduction is found around 5% higher in the  $408\mu m$  roughness length scale than those of  $337\mu m$ . Hence,  $k_G = 408\mu m$  (i.e., NSM20) is selected as an optimum representative roughness length scale in this study.

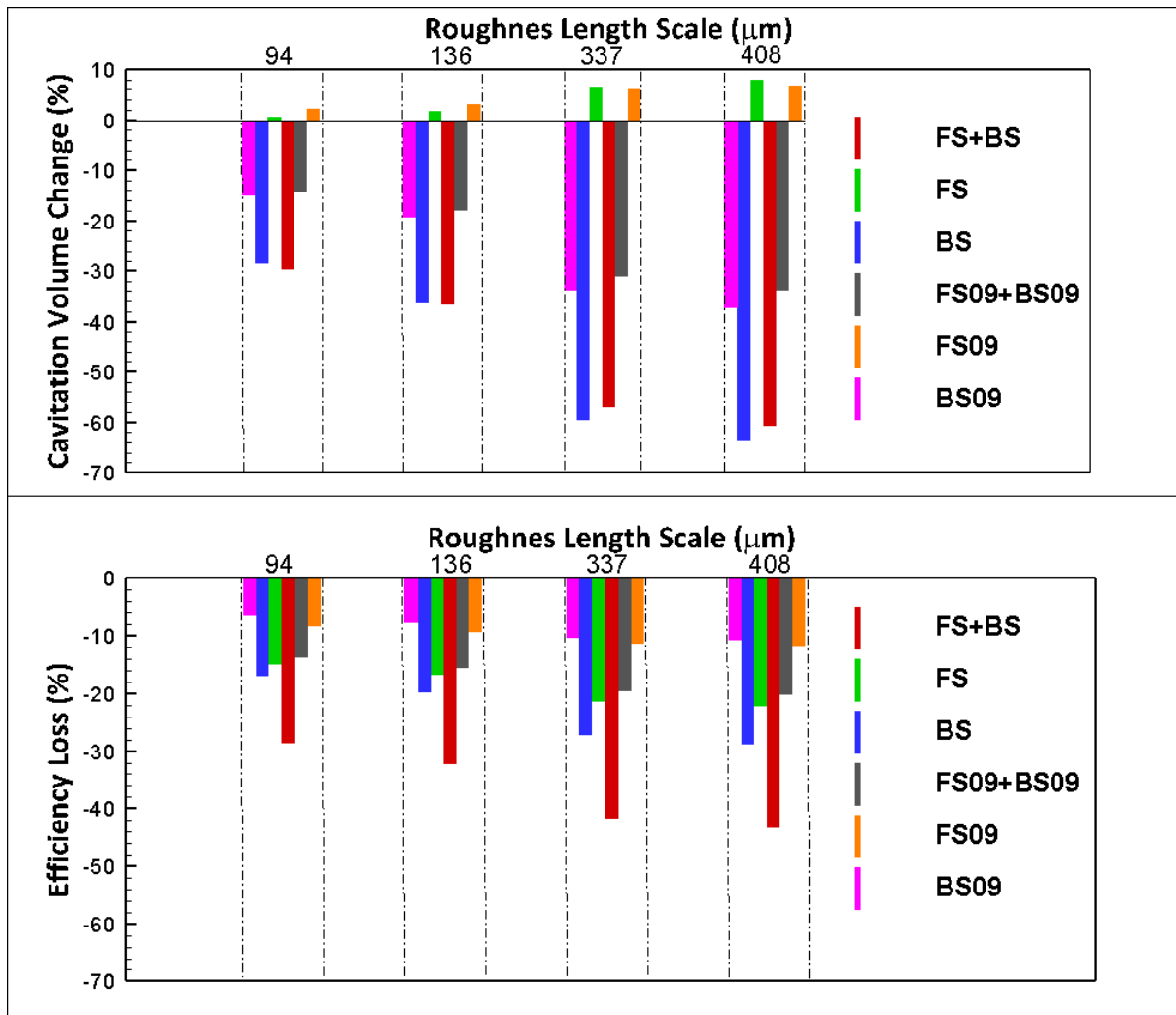


**Figure 10.** The variation of cavitation volume and efficiency with different roughness configurations and length scale with respect to smooth condition at C6.

As stated before, the roughness disrupts the tip vortex structure and provides TVC mitigation. For example, the comparison of TVC extension in the propeller slipstream between roughened and smooth propellers is given in Figure 11 for FS+BS and determined optimum roughness area (i.e., BS09) configurations. As shown in Figure 11, the more the roughness length scale, the more the TVC mitigation can be achieved for both configurations.

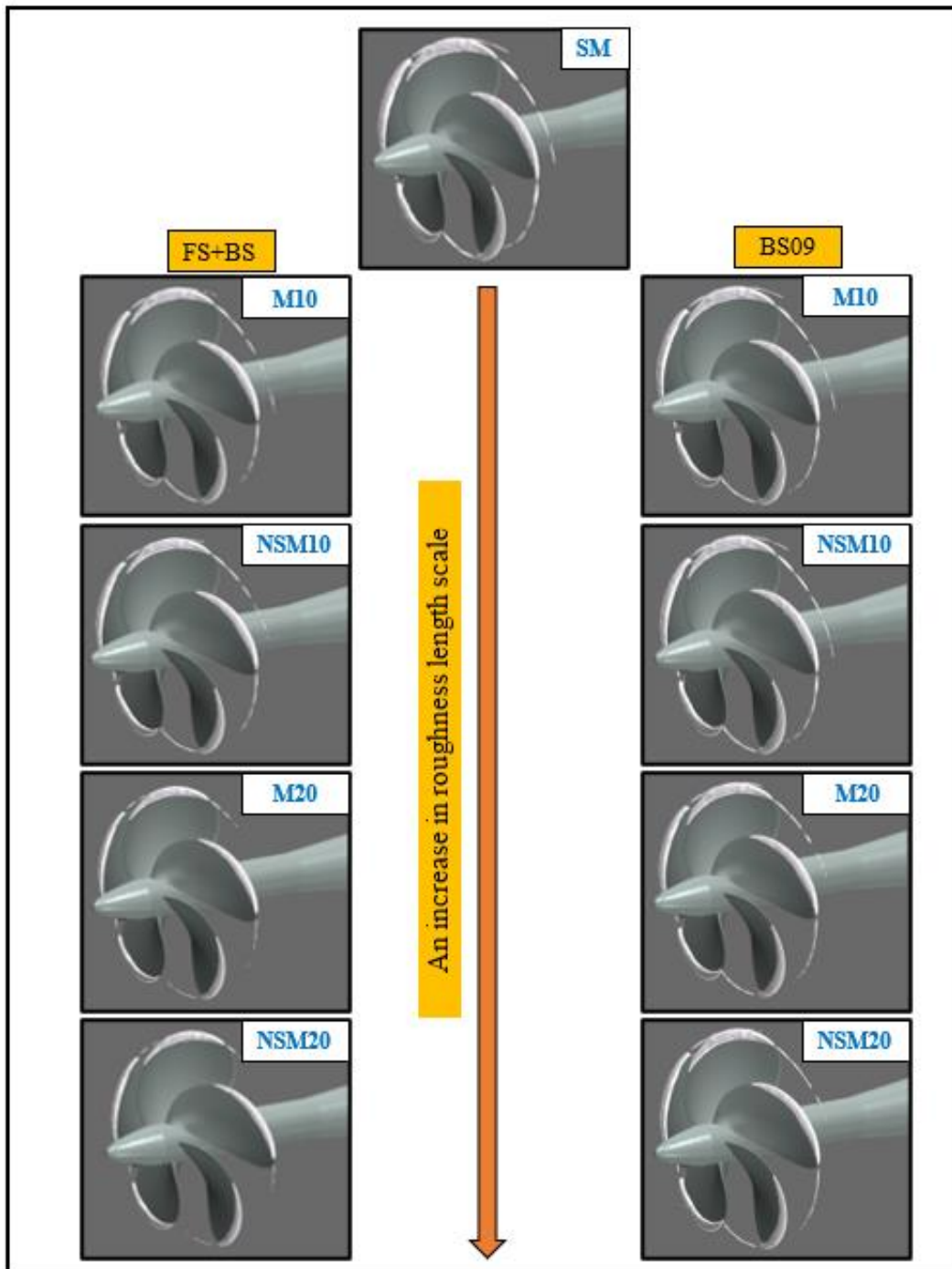
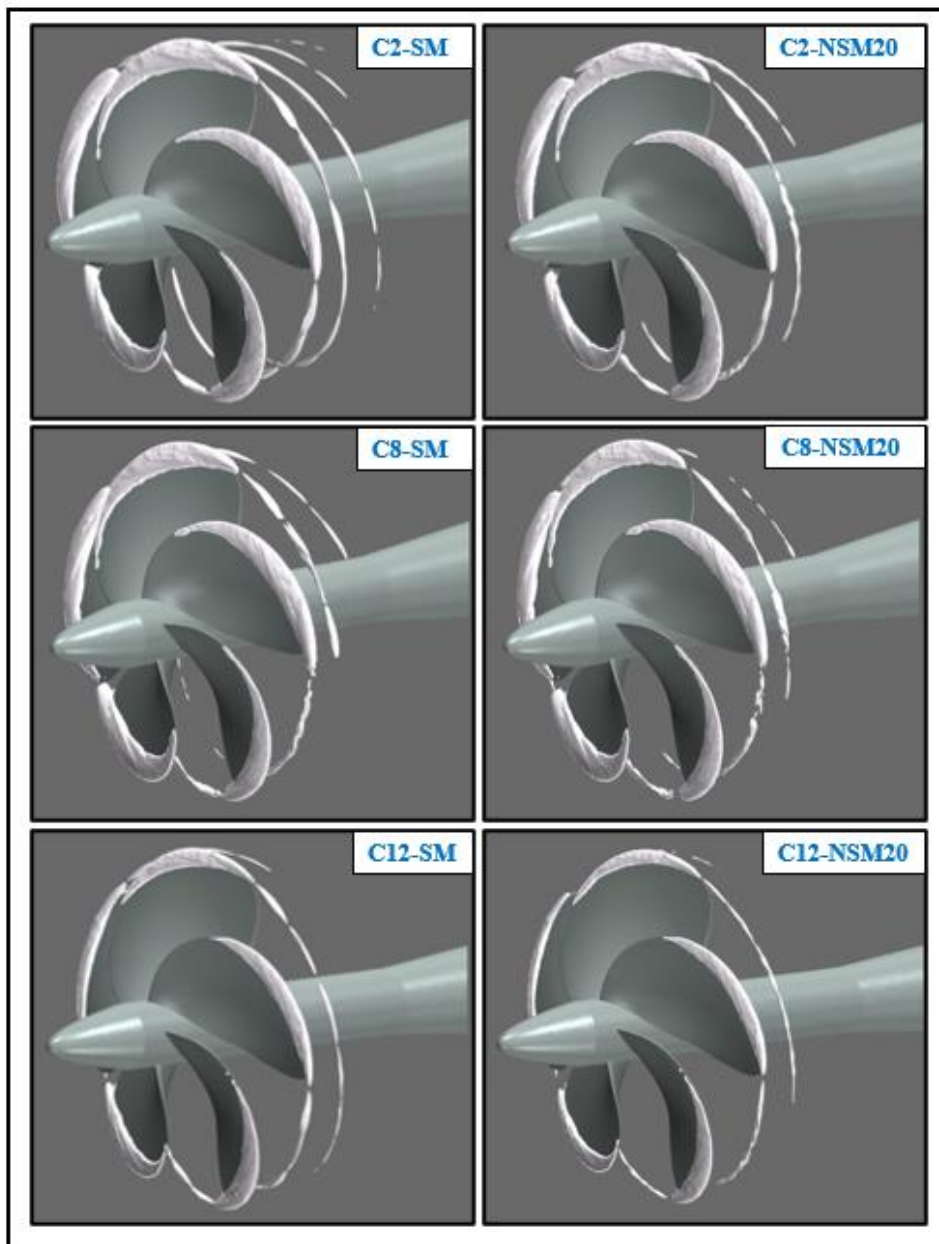


**Figure 11.** The change in TVC with an increase in roughness length scale at C6 ( $\alpha_v=0.1$ ).

### 5.2.1.3. Application of roughness on the optimum area using the optimum length scale for different operating conditions

The optimised roughness area (i.e., BS09) and the selected roughness length scale (i.e., NSM20,  $k_G = 408\mu m$ ) were tested for a wide range of operating conditions (i.e., C2, C8, C12 and C15) to show its effectiveness for the TVC mitigation and efficiency loss in model scale. Figure 12 shows the comparison of the cavitation extensions between the smooth and

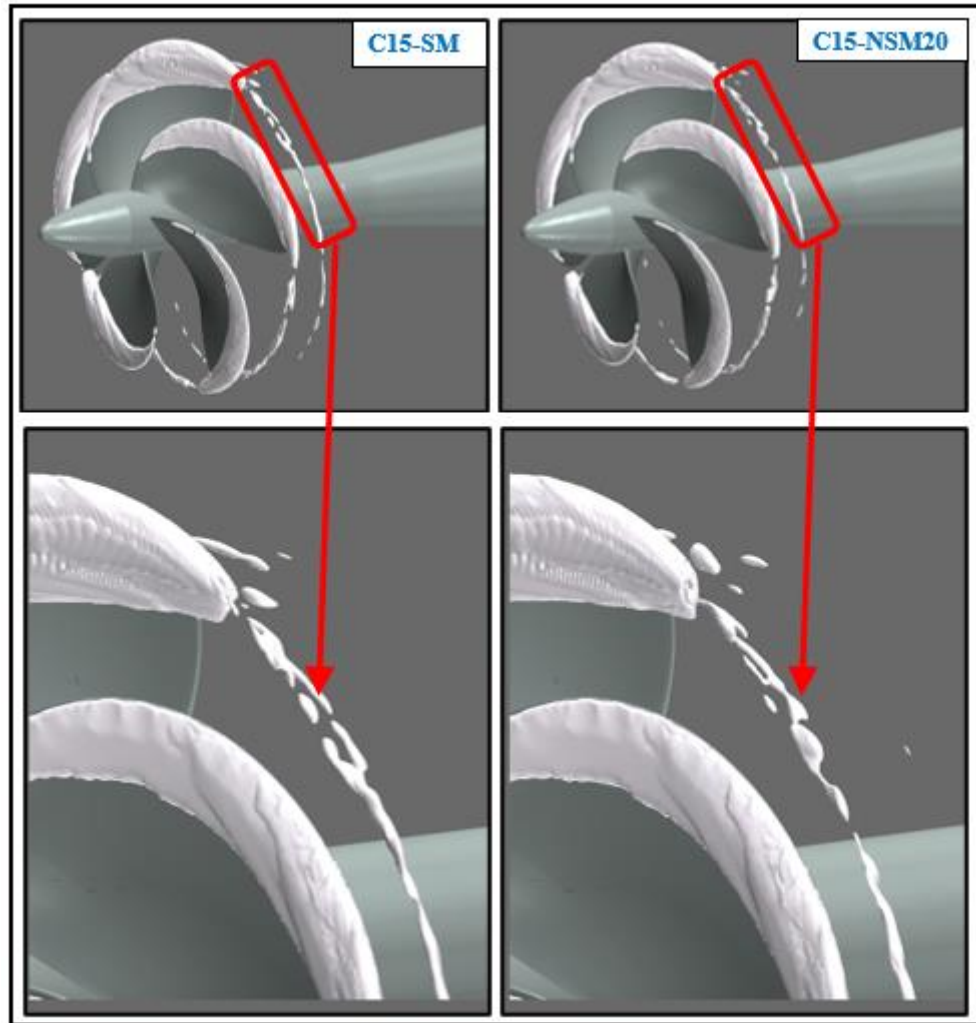
roughened blades. Akin to the C6, the roughness has a favourable impact on mitigating the stable and well-developed TVC emanating the blade tips under uniform (i.e., C2) and inclined flow conditions (i.e., C8 and C12) as given in Figure 12.



**Figure 12.** The change in TVC at different operational conditions in model scale ( $\alpha_v=0.1$ ).

Figure 13 also compares the variation of TVC between the roughened and smooth cases under non-uniform flow conditions. As shown in Figure 12, although the stable and structured TVC is observed under the uniform and inclined flow conditions, the tip vortex breaks up in the propeller slipstream. It presents somewhat different dynamics under the non-uniform flow conditions in comparison with the uniform flow conditions. This break-up phenomenon and complex structure and dynamics of TVC are disrupted with the roughness application

compared to a smooth case. Moreover, the strength of the first vortex formation, which occurs because of the sheet cavity break up, reduces with the roughness.



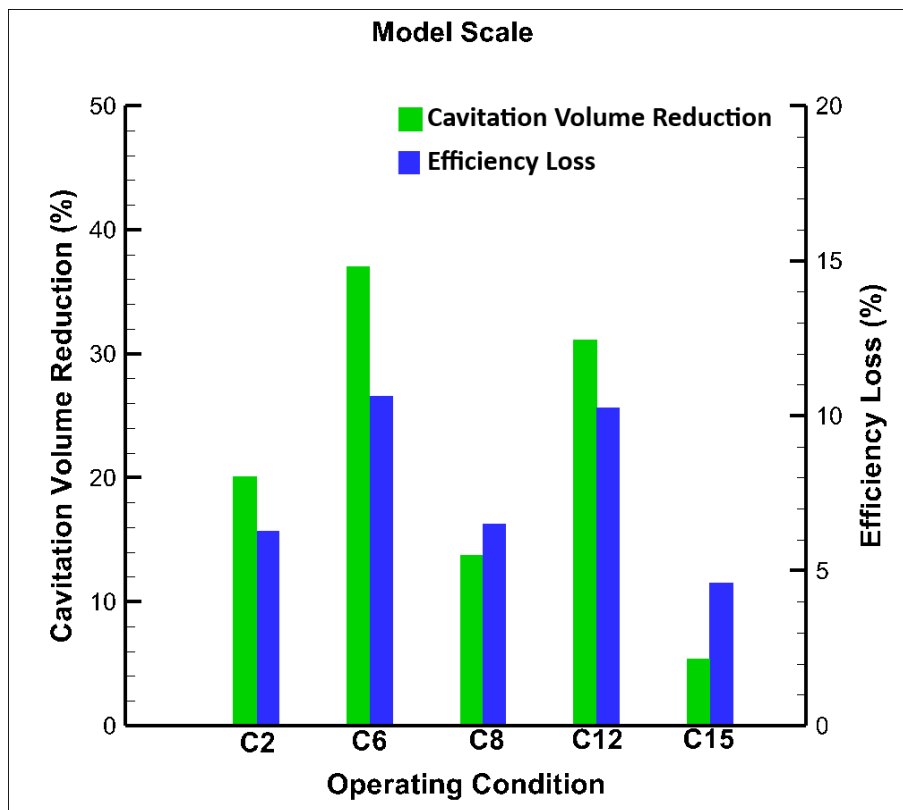
**Figure 13.** The variation of TVC structure with the roughness at C15 ( $\alpha_p=0.1$ ).

Table 9 shows the variation of the global performance characteristics in the presence of roughness with respect to the smooth condition. As shown in Table 9, the thrust coefficient decreases, whereas the torque coefficient increases with the application of roughness for all conditions. The maximum thrust reduction was 6.82% at C6, while the minimum torque increase was 1.53% at C2. The decrease in thrust and increase in torque coefficient leads to propeller efficiency loss, as shown in Figure 14. The maximum efficiency loss was found around 10% for C6 and C12 conditions. Contrary to the uniform and inclined flow conditions, the performance degradation was small under the non-uniform flow conditions (i.e., C15). Regarding the cavitation volume, the maximum reduction achieved was approximately %37 at C6. Although this is around 5% under non-uniform flow conditions (i.e., C15) in the

presence of roughness, the roughness also moderates the strength of the unstructured vortex, particularly in the roll-up process. Consequently, these results suggest that the overall cavitation volume reduction is greatly affected by roughness when operating in conditions where the stable and well-developed TVC is present (e.g., C2, C6, C8 and C12) as opposed to an unstructured and unstable TVC (e.g., C15).

**Table 9.** The change in thrust and torque coefficients in the presence of roughness with respect to smooth condition for model scale propeller.

Condition	$K_T$ (%)	$10K_Q$ (%)
C2	-4.85	1.53
C6	-6.82	4.25
C8	-4.66	1.99
C12	-6.70	3.97
C15	-3.03	1.69



**Figure 14.** The cavitation volume reduction and efficiency loss in the presence of roughness with respect to smooth conditions at different operating conditions in model scale.

### 5.2.2 Full-Scale Propeller

The optimum roughness area (i.e., BS09) was also used to investigate roughness effects on the full-scale propeller in terms of the performance degradation and mitigation of TVC at different operating conditions, as given in Tables 3 and 4. The scaling law for the roughness is dependent on the wall shear velocity at the propeller blade tips. This requires the selection of a larger roughness length scale in the model scale than the full-scale propeller. Yet, as stated in the study of Krüger et al., 2016, to represent the same hydrodynamic effects with roughness, the roughness height has to be almost the same order both in the model and full-scale propeller. Also, the geometric and dynamic similarity may not be possible between the model and full-scale propeller in the presence of roughness. Thus, the same representative roughness length scale (i.e., NSM20,  $k_G = 408\mu m$ ) was also used for the full-scale propeller.

Figure 15 shows the comparison of TVC between the smooth and roughened full-scale propellers under the uniform flow conditions at  $J=0.4$  and  $J=0.5$ , respectively. As shown in Figure 15, the suction side sheet cavitation covers a larger blade area at C13 (i.e.,  $J=0.4$ ) than those of C14 (i.e.,  $J=0.5$ ) because of the high blade loading. Also, an increase in blade loading deteriorates the TVC structure in the propeller slipstream in smooth condition. The stable and structured TVC is present at C14. However, this coherent vortex structure deteriorates with an increase in blade loading, which results in the variation of the TVC dynamics in the propeller slipstream. Similar to non-uniform flow conditions, two different vortex structures emanating the propeller blade tips are present at C13. Figure 16 also indicates the differences between the smooth and roughened full-scale propeller under non-uniform flow conditions. In all configurations, akin to the model scale operating conditions, the roughness weakens the tip vortex structure, and hence it provides TVC mitigation. Table 10 shows the change in thrust and torque coefficients in the presence of roughness with respect to the smooth condition. Unlike the model scale propeller, the increase in torque coefficient reduces for the full-scale propeller in the presence of roughness. However, inevitably, the thrust decrease results in efficiency loss for all operating conditions. The efficiency loss and cavitation volume reduction are given in Figure 17 in the presence of roughness. The results show that the efficiency loss predicted in the full-scale propeller is smaller than those of the model scale propeller.

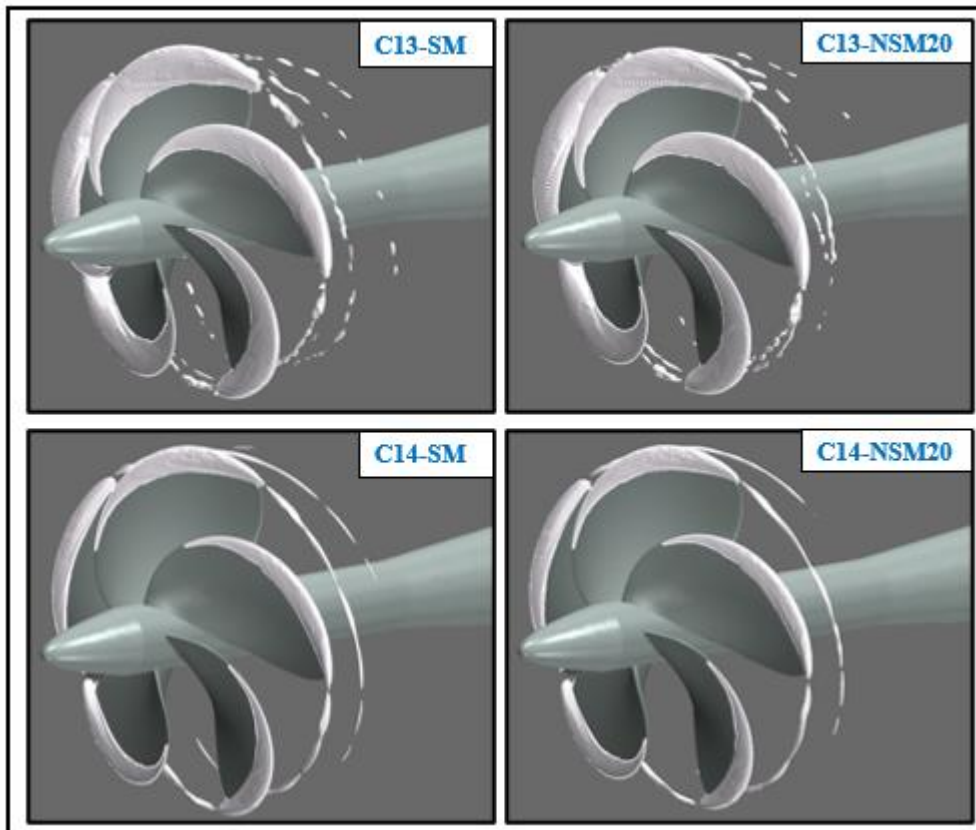


**Figure 15.** The change in TVC with the roughness under uniform flow conditions in full-scale ( $\alpha_v=0.1$ ).

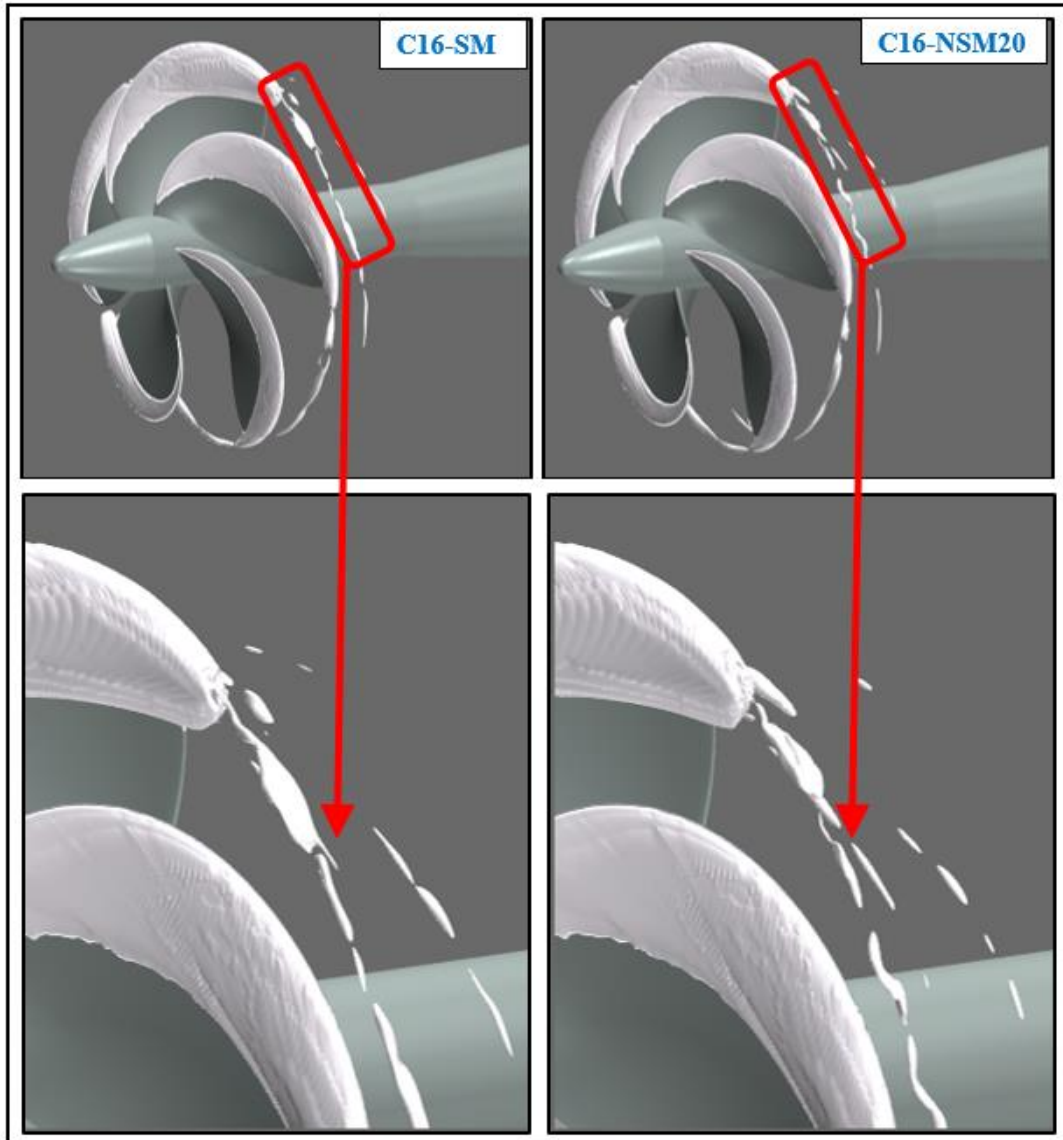


**Figure 16.** The change in TVC structure with the roughness at C16 ( $\alpha_v=0.1$ ).

**Table 10.** The change in thrust and torque coefficients in the presence of roughness with respect to smooth condition for the full-scale propeller.

Condition	$K_T$ (%)	$10K_Q$ (%)
C13	-2.05	0.38
C14	-5.87	0.06
C16	-2.80	0.28

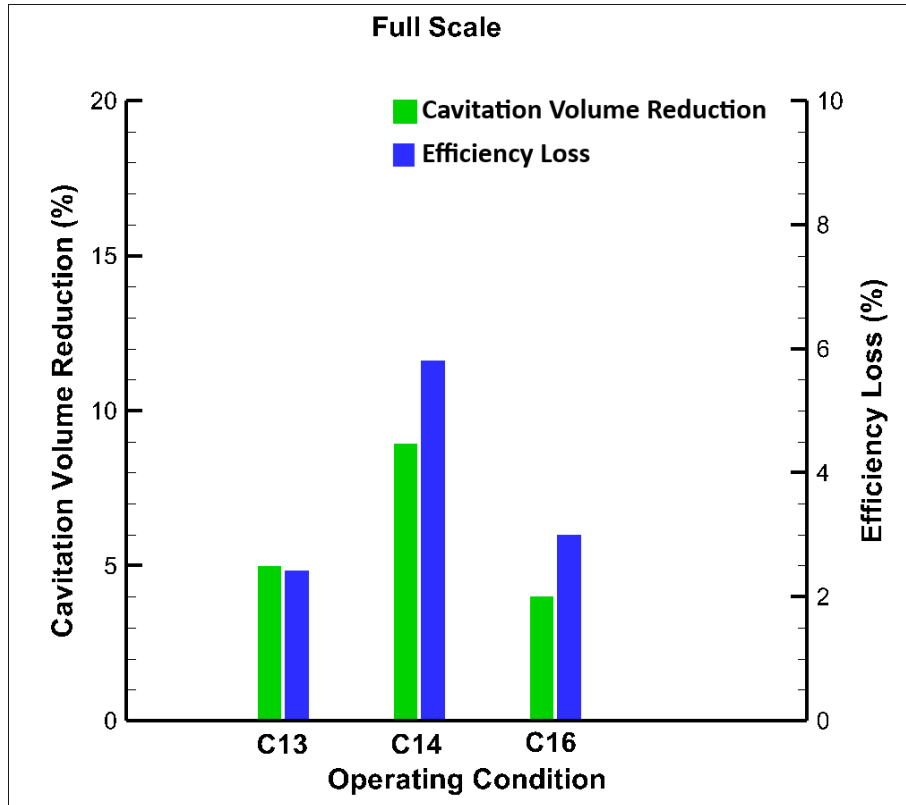


**Figure 17.** The cavitation volume reduction and efficiency loss in the presence of roughness with respect to smooth conditions at different operating conditions in full-scale.

## 6. Conclusions

In this study, the influence of the uniformly and non-uniformly distributed roughness on the propeller hydrodynamic performance, including the TVC, was investigated under uniform, inclined shaft, and non-uniform wake conditions. The investigations were focused on exploring the effect of the roughness on the propeller's global hydrodynamic performance as well as the strategic and effective use of the roughness to mitigate the TVC in the model and full-scale conditions. Based on these investigations, the following can be concluded as the main findings of this study:

- The roughened blade surfaces decreased the magnitude of the axial and tangential velocities inside the tip vortex. Also, the turbulent kinetic energy increased because of the momentum transfer in the presence of roughness. Thus, the pressure inside the tip vortex increased, resulting in the suppression of the TVC due to the roughness.
- Applying a uniformly distributed roughness pattern on the propeller blades provided maximum TVC mitigation. However, this also caused a substantial efficiency loss for the propeller due to the increased torque and decreased thrust. Therefore, it was concluded that the non-uniform (i.e., strategically and partially applied) distribution

of the roughness was critical to minimise the efficiency loss. Hence, the suction side (or backside) of the propeller blade tips (i.e.,  $0.9 \leq r/R \leq 1$ ) was found to be the strategically most favourable area to apply the roughness and minimise the efficiency loss.

- Applying the roughness on strategic areas on the propeller blades with optimum roughness length scale enabled considerable cavitation volume mitigation at the operating conditions where the stable and well-developed TVC dynamics are present. However, when the propeller operates in the condition where the unstable TVC dynamics are present, the strategic areas on the blades should be further optimised to mitigate the cavitation volume as similar to the condition where the stable TVC is present.
- The unfavourable impact of the roughness on the propeller efficiency was smaller in the full-scale propeller than that of the model-scale propeller under the uniform and inclined flow conditions.
- The results showed that the strategic application of the roughness not only changed the intensity of the TVC, particularly under the non-uniform flow conditions but also demonstrated the possibility of the TVC mitigation. Hence, the roughness can be an attractive passive noise control technique to mitigate the cavitation and, consequently, the cavitation induced URN for silent propeller designs.
- As a result of the above finding, this study has been extended further to explore the roughness effect on the cavitation induced propeller URN.

### Acknowledgements

The first author is sponsored by the Stone Marine Propulsion Ltd of the UK and the University of Strathclyde during his PhD study. Results were obtained using the ARCHIE-WeSt High-Performance Computer ([www.archie-west.ac.uk](http://www.archie-west.ac.uk)) based at the University of Strathclyde.

### References

- A. Feizi Chekab, M., Ghadimi, P., Reza Djeddi, S., Soroushan, M., 2013. Investigation of Different Methods of Noise Reduction for Submerged Marine Propellers and Their Classification. *Am. J. Mech. Eng.* 1, 34–42. <https://doi.org/10.12691/ajme-1-2-3>
- Aktas, B., Yilmaz, N., Atlar, M., Sasaki, N., Fitzsimmons, P., Taylor, D., 2020. Suppression of tip vortex cavitation noise of propellers using pressureporestm technology. *J. Mar. Sci. Eng.* 8. <https://doi.org/10.3390/jmse8030158>

- Andersson, J., Oliveira, D.R., Yeginbayeva, I., Leer-Andersen, M., Bensow, R.E., 2020. Review and comparison of methods to model ship hull roughness. *Appl. Ocean Res.* 99. <https://doi.org/10.1016/j.apor.2020.102119>
- Asnaghi, A., 2018. Computational Modelling for Cavitation and Tip Vortex Flows. PhD Thesis, Department of Mechanics and Maritime Sciences, Chalmers University of Technology.
- Asnaghi, A., Svennberg, U., Gustafsson, R., Bensow, R.E., 2020a. Investigations of tip vortex mitigation by using roughness. *Phys. Fluids* 32, 065111. <https://doi.org/10.1063/5.0009622>
- Asnaghi, A., Svennberg, U., Gustafsson, R., Bensow, R.E., 2020b. Propeller tip vortex mitigation by roughness application. *Appl. Ocean Res.* 102449. <https://doi.org/10.1016/j.apor.2020.102449>
- Asnaghi, A., Svennberg, U., Gustafsson, R., Bensow, R.E., 2020c. Investigations of tip vortex mitigation by using roughness. *Phys. Fluids* 32, 065111. <https://doi.org/10.1063/5.0009622>
- Atlar, M., Aktas, B., Samspon, R., Fitzsimmons, P., Fetherstonhaug, C., 2013. A multi-purpose marine science and technology research vessel for full-scale observations and measurements, 3rd International Conference on Advanced Model Measurement Technologies for the Marine Industry, 'AMT'13. Gdansk, Poland.
- Bosschers, J., 2018. Propeller Tip-Vortex Cavitation and its Broadband Noise, PhD Thesis, The University of Twente.
- Carlton, J., 2018. *Marine Propellers and Propulsion - 4th Edition*. Butterworth-Heinemann.
- Chahine, G.L., Frederick, G.F., Bateman, R.D., 1993. Propeller tip vortex cavitation suppression using selective polymer injection. *J. Fluids Eng. Trans. ASME* 115, 497–503. <https://doi.org/10.1115/1.2910166>
- Colebrook, CF, 1939. Turbulent Flow in Pipes, with particular reference to the transition region between the smooth and rough pipe laws. *J. Inst. Civ. Eng.* 11, 133–156. <https://doi.org/10.1680/ijoti.1939.13150>
- Fruman, DH, Aflalo, SS, 1989. Tip vortex cavitation inhibition by drag-reducing polymer solutions. *J. Fluids Eng. Trans. ASME* 111, 211–216. <https://doi.org/10.1115/1.3243625>
- Grigson, C., 1992. Drag Losses of New Ships Caused by Hull Finish. *J. Ship. Res.* 36, 182–196.
- Hildebrand, J., 2004. Sources of anthropogenic sound in the marine environment, International Policy Workshop on Sound and Marine Mammals. London, UK.
- Johnsson, C.A., Rutgersson, O., 1991. LEADING EDGE ROUGHNESS - A WAY TO IMPROVE PROPELLER TIP VORTEX CAVITATION, Propeller Shafting Symposium. Virginia Beach, VA, USA, pp. 1–12.
- Katz, J., Galdo, JB, 1989. Effect of roughness on roll-up of tip vortices on a rectangular hydrofoil. *J. Aircr.* 26, 247–253. <https://doi.org/10.2514/3.45753>
- Konno, A., Wakabayashi, K., Yamaguchi, H., Maeda, M., Ishii, N., Soejima, S., Kimura, K., 2002. On the mechanism of the bursting phenomena of propeller tip vortex cavitation. *J. Mar. Sci. Technol.* 6, 181–192. <https://doi.org/10.1007/s007730200006>
- Korkut, E., Atlar, M., 2012. An experimental investigation of the effect of foul release coating application on performance, noise and cavitation characteristics of marine propellers. *Ocean Eng.* 41, 1–12. <https://doi.org/10.1016/j.oceaneng.2011.12.012>
- Korkut, E., Takinaci, A.C., 2013. 18M Research Vessel Wake Measurements. Istanbul, Turkey.
- Krüger, C., Kornev, N., Greitsch, L., 2016. Influence of propeller tip roughness on tip vortex strength and propeller performance. *Sh. Technol. Res.* 63, 110–120. <https://doi.org/10.1080/09377255.2016.1205293>

- Kuiper, G., 1981. Cavitation inception on ship propeller models. PhD Thesis, Delft University of Technology.
- Lorenzo, F. De, Tomàs, A.O., White, P.R., 2017. Underwater noise limits and measurement of underwater radiated noise from merchant vessels, 24th International Congress on Sound and Vibration, ICSV 2017. London, UK.
- McKenna, M.F., Ross, D., Wiggins, S.M., Hildebrand, J.A., 2012. Underwater radiated noise from modern commercial ships. *J. Acoust. Soc. Am.* 131, 92–103. <https://doi.org/10.1121/1.3664100>
- Platzer, G.P., Souders, W.G., 1981. Tip vortex cavitation characteristics and delay of inception on a three-dimensional hydrofoil / by William G. Souders, Gregory P. Platzer., DTNSRDS-81/007. David W. Taylor Naval Ship Research and Development Center, Bethesda, Md. : <https://doi.org/10.5962/bhl.title.47554>
- Platzer, G.P., Souders, W.G., 1979. Tip vortex cavitation delay with application to marine lifting surfaces, DTNSRDC Technical report 79/051. David W. Taylor Naval Ship Research and Development Center, Bethesda, Md. : <https://doi.org/10.5962/bhl.title.47556>
- Sampson, R., Turkmen, S., Aktas, B., Shi, W., Fitzsimmons, P., Atlar, M., 2015. On the full scale and model scale cavitation comparisons of a Deep-V catamaran research vessel, in: Fourth International Symposium on Marine Propulsors, 'SMP'15. Austin, Texas, USA.
- Schnerr, G.H., Sauer, J., 2001. Physical and Numerical Modeling of Unsteady Cavitation Dynamics, in: 4th International Conference on Multiphase Flow, ICMF-2001. New Orleans, USA.
- Schultz, M.P., Swain, G.W., 2000. The influence of biofilms on skin friction drag. *Biofouling* 15, 129–139. <https://doi.org/10.1080/08927010009386304>
- Sezen, S., Atlar, M., 2021. An Alternative Vorticity based Adaptive Mesh Refinement Technique for Tip Vortex Cavitation Modelling using RANS, DES and LES methods. *Ship Technology Research*, <https://doi.org/10.1080/09377255.2021.1927590>.
- Sezen, S., Uzun, D., Ozyurt, R., Turan, O., Atlar, M., 2021. Effect of biofouling roughness on a marine propeller's performance including cavitation and underwater radiated noise (URN). *Appl. Ocean Res.* 107, 102491. <https://doi.org/10.1016/j.apor.2020.102491>
- SONIC, 2012. Suppression Of underwater Noise Induced by Cavitation EC-FP7, Grant Agreement No: 2012 314394.
- Spalart, P.R., Deck, S., Shur, M.L., Squires, K.D., Strelets, M.K., Travin, A., 2006. A new version of detached-eddy simulation, resistant to ambiguous grid densities. *Theor. Comput. Fluid Dyn.* 20, 181–195. <https://doi.org/10.1007/s00162-006-0015-0>
- Star CCM+, 2019. User Guide.
- Svennberg, U., Asnaghi, A., Gustafsson, R., Bensow, R.E., 2020. Experimental Analysis of Tip Vortex Cavitation Mitigation By Controlled Surface Roughness. *J. Hydrodyn.* 2020 1–12. <https://doi.org/10.1007/s42241-020-0073-6>
- Tani, G., Aktas, B., Viviani, M., Yilmaz, N., Miglianti, F., Ferrando, M., Atlar, M., 2019a. Cavitation tunnel tests for "The Princess Royal" model propeller behind a 2-dimensional wake screen. *Ocean Eng.* 172, 829–843. <https://doi.org/10.1016/j.oceaneng.2018.11.017>
- Tani, G., Viviani, M., Felli, M., Lefeber, F.H., Lloyd, T., Aktas, B., Atlar, M., Turkmen, S., Seol, H., Hallander, J., Sakamoto, N., 2020. Noise measurements of a cavitating propeller in different facilities: Results of the round-robin test programme. *Ocean Eng.* 213, 107599. <https://doi.org/10.1016/j.oceaneng.2020.107599>
- Tani, G., Viviani, M., Felli, M., Lefeber, F.H., Lloyd, T., Atlar, M., Seol, H., Hallander, J.,

- Sakamoto, N., Kamiirisa, H., 2019b. Round Robin Test on Radiated Noise of a Cavitating Propeller, Proceedings of 6th International Symposium on Marine Propulsors, SPM'19. Rome, Italy.
- UNCTAD, 2019. Review of Maritime Transport, United Nations.
- Uzun, D., Ozyurt, R., Demirel, Y.K., Turan, O., 2020. Does the barnacle settlement pattern affect ship resistance and powering? Appl. Ocean Res. 95, 102020. <https://doi.org/10.1016/j.apor.2019.102020>
- Yakushiji, R., 2009. Mechanism of Tip Vortex Cavitation Suppression by Polymer and Water Injection. PhD Thesis, Naval Architecture and Marine Engineering, University of Michigan.